Path integral Monte Carlo study of one-dimensional Bose system: Luttinger liquid properties and impurity effects

Lunić, Frane

University of Split
Faculty of Science

Path integral Monte Carlo study of one-dimensional Bose system: Luttinger liquid properties and impurity effects

Master thesis

Frane Lunić

Split, September 2017

Temeljna dokumentacijska kartica

Sveučilište u Splitu
Prirodoslovno – matematički fakultet
Odjel za fiziku
Ruđera Boškovića 33, 21000 Split, Hrvatska

Diplomski rad

Istraživanje jednodimenzionalnih bozonskih sustava metodom integrala po stazama: osobine Luttingerove tekućine i utjecaj nečistoća

Frane Lunić

Sveučilišni diplomski studij Fizika, smjer Računarska fizika

Sažetak:

Predstavljamo rezultate studije jednodimenzionalnih, uniformnih i neuređenih sustava interagirajućih bozona, izvršene numeričkom Monte Carlo metodom integrala po stazama (PIMC metoda). Interes za ovu vrstu sustava je porastao nedavno otkad su eksperimentalno ostvareni u polju ultrahladnih atomskih plinova te adsorpcijom u uskim nanoporama. Nakon opisa teorijske pozadine i metoda predstavljamo rezultate, fokusirajući se na udio suprafluida, jednočestičnu matricu gustoće i korelacijsku funkciju parova, te ih uspoređujemo s predviđanjima teorije Luttingerove tekućine (LL). U slučaju uniformnih sustava, pronalazimo slaganje te određujemo Luttingerov parametar K na više načina. Nakon dodavanja nečistoće na nasumičnom položaju u sustav, za $K < 1$ nismo pronašli skaliranje udjela suprafluida s LT, što je vjerojatno znak lokalizacije predviđene u LL teoriji. Za $K > 1$ smo pronašli skaliranje što predstavlja očekivanu kvalitativnu razliku, ali rezultati pokazuju zanimljiva odstupanja od očekivane relacije skaliranja. U radu smo diskutirali moguća objašnjenja.

Ključne riječi: 1D, Luttingerova tekućina, nered, suprafluidnost, lokalizacija, kvantni Monte Carlo

Rad sadrži: 59 stranica, 20 slika, 0 tablica, 29 literaturnih navoda. Izvornik je na engleskom jeziku.

Mentor: Dr. sc. Leandra Vranješ Markić, redoviti profesor Prirodoslovno-matematičkog fakulteta, Sveučilišta u Splitu

Ocjenjivači: Dr. sc. Leandra Vranješ Markić, redoviti profesor Prirodoslovno-matematičkog fakulteta, Sveučilišta u Splitu
Dr. sc. Franjo Sokolić, redoviti profesor Prirodoslovno-matematičkog fakulteta, Sveučilišta u Splitu
Dr. sc. Petar Stipanović, viši asistent Prirodoslovno-matematičkog fakulteta, Sveučilišta u Splitu

Rad prihvaćen: 29. rujna. 2017.

Rad je pohranjen u Knjižnici Prirodoslovno – matematičkog fakulteta, Sveučilišta u Splitu.

Basic documentation card

University of Split
Faculty of Science
Department of Physics
Ruđera Boškovića 33, 21000 Split, Croatia

Master thesis

Path integral Monte Carlo study of one-dimensional Bose system: Luttinger liquid properties and impurity effects

Frane Lunić

University graduate study programme Physics, orientation Computational Physics

Abstract:

We present the results of a numerical path integral Monte Carlo (PIMC) study of one-dimensional uniform and disordered systems of interacting bosons. The interest in this kind of systems has grown recently since they have been realized experimentally in the field of ultracold atomic gases, as well as by adsorption of atoms in narrow nanopores. After providing theoretical background and laying out the methods, we present the results, with focus on superfluid fraction, OBDM, and pair-correlation function, and compare them with the predictions of the Luttinger liquid theory (LL). In case of uniform systems, we find agreement. The Luttinger parameter K is determined in several ways. After adding a randomly placed impurity to the system, for $K < 1$ we find no scaling of superfluid fraction with LT, most likely signifying localization, as predicted by LL. Scaling is found for $K > 1$, indicating a qualitative difference, expected from LL. However, interesting deviations from the expected scaling relation are found. Possible explanations are discussed.

Keywords: 1D, Luttinger liquid, disorder, superfluidity, localization, quantum Monte Carlo

Thesis consists of: 59 pages, 20 figures, 0 tables, 29 references. Original language: English.

Supervisor: Leandra Vranješ Markić, Ph.D., Professor at the Faculty of Science, University of Split

Reviewers: Leandra Vranješ Markić, Ph.D., Professor at the Faculty of Science, University of Split
Franjo Sokolić, Ph.D., Professor at the Faculty of Science, University of Split
Petar Stipanović, Ph.D., Senior instructor at the Faculty of Science, University of Split

Thesis accepted: September 29, 2017

Thesis is deposited in the library of the Faculty of Science, University of Split.

Contents

Chapter 1

Introduction

The topic of this thesis is exploration of properties of certain one-dimensional systems obeying Bose statistics. We touch upon many concepts of interest in condensed matter and ultra-cold gas physics, such as superfluidity, Bose-Einstein condensation and the Tomonaga-Luttinger theory of one-dimensional systems.

One-dimensional systems are not necessarily only toy models, and they can be fundamentally different from, and no less difficult to understand than higher-dimensional systems, as theories highly successful in three dimensions tend to fail in one [9]. The difference is clearly visible from the fact that perturbations can only give rise to collective excitations since there is no way for particles to move around each other. The Tomonaga-Luttinger liquid theory is a low-energy one-dimensional theory that successfully describes the physics of various simple one-dimensional systems [9]. It has been experimentally realised in cold atomic and other systems [25].

Aside from purely theoretical interest, the motivation for studying low-dimensional systems stems from the possibility of their realization in various conditions. An example of this is the design of materials in such manner that movement of electrons becomes restricted in one or more directions, which can result in quantization effects that preclude motion in the restricted dimensions [25]. In fact, most of the early research of one-dimensional systems was concerned with electrons, since the study of electronic properties of quasi one-dimensional materials has a clear potential for application. However, the distinction between Bose and Fermi systems is not always clear cut. Cooper pairs behave to an extent as bosons [19], and the nature of one-dimensional systems prevents the exchange of particles without collision, which reduces the distinction between Bose and Fermi statistics [11]. The considerable overlap between results on Bose and Fermi systems is part of the motivation for studying one-dimensional Bose systems, and the relatively recent experimental developments have encouraged more theoretical activity in this field. These developments include confinement of cold atoms in essentially one-dimensional anisotropic traps, optical lattices, and elongated pores [19]. The properties of these

systems can be modified by changing experimental conditions. For example, a uniform magnetic field can be applied to control interactions via Feshbach resonances and optical lattices can be used to test theories of condensed matter physics [7].

Disordered systems are a topic of much interest in condensed matter physics, since lattice imperfections and impurities are almost inescapable, and give rise to phenomena such as resistivity. It has been shown that disorder can have a profound effect on conductive or superfluid properties of one-dimensional systems. It causes localization of eigenstates in noninteracting systems and the competition between superfluidity and localization in normally superfluid systems [18, 19, 25]. Localization in presence of disorder has been confirmed numerically and experimentally [25], but details are still a topic of research. The results on the effect of disorder on superfluidity of a recent numerical study of $^4\mathrm{He}$ atoms in narrow pores [17] show signs of localization, but only when extrapolated to system sizes larger than those simulated, and apparent disagreement with the prediction on the domain of validity of the Tomonaga-Luttinger liquid regime (see [19, 22]). It is our primary aim to further research this aspect, and we present here the results and discussion of a similar study on disorder and superfluidity, the main difference being that simulations are performed in pure one-dimensional instead of quasi one-dimensional geometry.

This thesis is organized as follows. In chapter 2 we give a brief and cursory overview of the relevant physical theory. First we discuss topics of quantum statistical mechanics, Bose-Einstein condensation, and superfluidity. Then we present the path integral formalism in quantum mechanics, and its application to quantum statistical mechanics, along with derivation of the relation between superfluidity and imaginary-time path winding around the periodic boundaries of the system. We conclude this chapter with discussion of one-dimensional quantum systems. In chapter 3 we present the specifics of the simulated systems and outline the procedure followed, after which we discuss some of the general aspects of the path integral Monte Carlo method, and some of the more specific aspects of the worm algorithm implementation that we have used. Following this, in chapter 4 we present the obtained results on correlation functions and fractions of superfluid in systems with and without disorder. The results are further discussed in chapter 5, and final summary of conclusions is given in chapter 6.

Chapter 2

Theory

In this chapter we present the theory behind the studied phenomena and methods used in the study. We begin by covering some theory in the background of the more directly relevant one-dimensional theory. This includes the Bose-Einstein condensation and superfluidity, phenomena of interest to both physics of ultra-cold gases, and condensed matter physics. The path integral formalism, which is of interest to many branches of physics, is also introduced. We will assume particles are spinless throughout this chapter, and the remainder of this thesis.

2.1 Theoretical background

2.1.1 Density matrix and quantum statistical mechanics

Suppose a system is in a pure quantum state $|\phi\rangle$. The projection operator is defined as $|\phi\rangle\langle\phi|$, and its expectation value in the state $|\psi\rangle$ is the probability of a measurement yielding the state $|\psi\rangle$. This probability depends on the overlap of the two states, hence the projection of one onto another. Suppose now our system is a statistical mixture of states (a mixed state), that is, it can occupy any of the states $|\phi_i\rangle$ with probabilities given by p_i.[1] We may generalize the projection operator in the following manner.Let the set of $|\phi_i\rangle$ be a complete set of orthonormal vectors. We define the density matrix as [1]

$$\widehat{\rho} = \sum_i p_i \left|\phi_i\right\rangle\!\left\langle\phi_i\right| . \tag{2.1}$$

[1]This is different from quantum superposition. A pure state can be a superposition of multiple states, but a mixed state is not a superposition of pure states. Mixed states arise as a consequence of the uncertainty due to interaction with the environment.

If all probabilities are zero except for $p_j = 1$, the pure state and the simple projection operator are recovered. [2]

If $\langle\phi_i|\widehat{O}|\phi_i\rangle$ is the expectation value of the operator $\widehat{O}$ in the state ϕ_i, the mixed state expectation value is given by

$$\langle\widehat{O}\rangle = \sum_i p_i \langle\phi_i|\widehat{O}|\phi_i\rangle . \tag{2.2}$$

It can be shown by inserting the unit operator $\sum_j |\phi_j\rangle\langle\phi_j|$ to the right of $\widehat{O}$ in (2.2) and using commutative and distributive properties that

$$\langle\widehat{O}\rangle = \sum_j \langle\phi_j|\widehat{\rho}\widehat{O}|\phi_j\rangle \equiv \mathrm{Tr}\,\widehat{\rho}\widehat{O}. \tag{2.3}$$

Let the system be composed of N particles, and let $\boldsymbol{R} = \{\boldsymbol{r}_1, \boldsymbol{r}_2, ..., \boldsymbol{r}_N\}$ represent a configuration of the system's coordinates. The density matrix elements in coordinate representation are given as

$$\rho(\boldsymbol{R}, \boldsymbol{R}') = \langle\boldsymbol{R}|\widehat{\rho}|\boldsymbol{R}'\rangle = \sum_i p_i\, \phi_i(\boldsymbol{R})\phi_i^*(\boldsymbol{R}'), \tag{2.4}$$

where $|\boldsymbol{R}\rangle$ and $|\boldsymbol{R}'\rangle$ are states of different definite configurations of coordinates, and $\langle\boldsymbol{R}|\,\phi_i\rangle = \phi_i(\boldsymbol{R})$. The diagonal element $\rho(\boldsymbol{R}, \boldsymbol{R}) \equiv \rho(\boldsymbol{R})$ is the probability of finding the system in the configuration $\boldsymbol{R}$. The expectation value in the coordinate representation is

$$\langle\widehat{O}\rangle = \mathrm{Tr}\,\widehat{\rho}\widehat{O} = \int \mathrm{d}\boldsymbol{R}\ \langle\boldsymbol{R}|\widehat{\rho}\widehat{O}|\boldsymbol{R}\rangle . \tag{2.5}$$

By inserting the unit operator $\int \mathrm{d}\boldsymbol{R}'\, |\boldsymbol{R}'\rangle\langle\boldsymbol{R}'|$ between the two operators on the right hand side of (2.5) we obtain the expression [1, 3]

$$\langle\widehat{O}\rangle = \int \mathrm{d}\boldsymbol{R}\,\mathrm{d}\boldsymbol{R}'\,\rho(\boldsymbol{R}, \boldsymbol{R}')\,\langle\boldsymbol{R}'|\widehat{O}|\boldsymbol{R}\rangle \tag{2.6}$$

We can now introduce the reduced p-body density matrices by integrating out coordinates $\boldsymbol{r}_{i>p}$ and multiplying with the normalization factor $\frac{N!}{(N-p)!}$.[3] The reduced density matrices can be used to calculate expectation values of p-body operators (e.g. the two body potential) in a manner analogous to (2.6). The one-body density matrix (OBDM)

$$\rho(\boldsymbol{r}, \boldsymbol{r}') = N \int \mathrm{d}\boldsymbol{r}_2 \cdots \mathrm{d}\boldsymbol{r}_N\, \rho(\{\boldsymbol{r}_1, \boldsymbol{r}_2, ..., \boldsymbol{r}_N\}, \{\boldsymbol{r}_1', \boldsymbol{r}_2, ..., \boldsymbol{r}_N\}) \tag{2.7}$$

is of the most interest for this thesis. By setting $\boldsymbol{r} = \boldsymbol{r}'$, we obtain the particle density

[2] It can be shown that the necessary and sufficient condition for a pure state is that the density matrix is idempotent, meaning $\rho^2 = \rho$.

[3] The particular normalization is convenient in the second quantization framework, but there are multiple normalization conventions as laid out in [4].

$n(\boldsymbol{r}) \equiv \rho(\boldsymbol{r}, \boldsymbol{r})$.

Suppose the system of interest is in equilibrium with a heat bath, kept at a fixed temperature, volume and number of particles (the canonical ensemble), and let $\widehat{H}$ be the Hamiltonian of the system. The probability of a microstate $|\phi_i\rangle$ associated with the energy eigenvalue E_i is

$$p_i = \frac{e^{-\beta E_i}}{Z}, \tag{2.8}$$

Z being the partition function

$$Z = \sum_i e^{-\beta E_i} = \operatorname{Tr} e^{-\beta \widehat{H}}. \tag{2.9}$$

Now the density matrix takes the form

$$\widehat{\rho} = \frac{1}{Z} \sum_i e^{-\beta E_i} \, |\phi_i\rangle\langle\phi_i| = \frac{e^{-\beta \widehat{H}}}{Z} \sum_i |\phi_i\rangle\langle\phi_i| \,, \tag{2.10}$$

and finally [1, 3]

$$\widehat{\rho} = \frac{e^{-\beta \widehat{H}}}{Z}. \tag{2.11}$$

In this case, it is useful to denote the density matrix with β, as in $\rho(\boldsymbol{R}, \boldsymbol{R}'; \beta)$.

It can be shown by differentiating an element $\rho_{ij} = \delta_{ij} e^{-\beta E_i}$ of the density matrix (2.11) that $\widehat{\rho}(\beta)$ satisfies the equation

$$-\frac{\partial \widehat{\rho}(\beta)}{\partial \beta} = \widehat{H} \widehat{\rho}. \tag{2.12}$$

In case of a one-dimensional particle, (2.12) is a simple diffusion equation

$$-\frac{\partial \rho(x, x'; \beta)}{\partial \beta} = -\lambda \frac{\partial^2}{\partial x^2} \rho(x, x'; \beta), \tag{2.13}$$

where $\lambda = \frac{\hbar^2}{2m}$. The initial condition can be chosen as $\rho(x, x'; 0) = \delta(x - x')$ [4], and the solution is given by

$$\rho(x, x'; \beta) = (4\pi\lambda\beta)^{-1/2} \, \exp\left[-\frac{(x - x')^2}{4\lambda\beta}\right] \tag{2.14}$$

Generalizing to N three-dimensional particles, we have

$$\rho(\boldsymbol{R}, \boldsymbol{R}'; \beta) = (4\pi\lambda\beta)^{-3N/2} \exp\left[-\frac{(\boldsymbol{R} - \boldsymbol{R}')^2}{4\lambda\beta}\right]. \tag{2.15}$$

This equation can be applied to the case of particles in a box, as long as thermal wavelength

[4] This corresponds to perfect localization of the particle at infinite kinetic energy, and therefore, zero de Broglie wavelength.

$\Lambda_T = \sqrt{2\beta\lambda}$ is much less than the size of the box [3].

Symmetrized density matrix

So far, we have dealt only with distinguishable particles. More realistic systems of indistinguishable particles can only occupy states that are either symmetric or antisymmetric with respect to the exchange of particles.

Let $\mathcal{P}$ be a permutation of particle labels, so that $\mathcal{P}\boldsymbol{R} = \{\boldsymbol{r}_{\mathcal{P}_1}, \boldsymbol{r}_{\mathcal{P}_2}, \ldots, \boldsymbol{r}_{\mathcal{P}_N}\}$. We have $\phi_\pm(\mathcal{P}\boldsymbol{R}) = (\pm 1)^{\mathrm{sgn}\,\mathcal{P}}\phi(\boldsymbol{R})$, where the index + denotes the symmetric, and - antisymmetric state. Let us define symmetrization and antisymmetrization operators by

$$\widehat{\mathcal{P}}_\pm\,\phi(\boldsymbol{R}) = \frac{1}{N!}\sum_{\mathcal{P}}(\pm 1)^{\mathrm{sgn}\,\mathcal{P}}\phi(\mathcal{P}\boldsymbol{R}). \tag{2.16}$$

It can be shown from group theory that when the operators act on an arbitrary state they project out (anti)symmetric states [1, 3]. This allows us to construct Bose or Fermi density matrix from the density matrix of distinguishable particles (2.4),

$$\rho_\pm(\boldsymbol{R}, \boldsymbol{R}'; \beta) \equiv \widehat{\mathcal{P}}_\pm\,\rho_D(\boldsymbol{R}, \boldsymbol{R}'; \beta)) = \frac{1}{N!}\sum_{\mathcal{P}}(\pm 1)^{\mathrm{sgn}\,\mathcal{P}}\rho_D(\boldsymbol{R}, \mathcal{P}\boldsymbol{R}'; \beta). \tag{2.17}$$

Since we are interested in Bose systems, we will denote $\widehat{\mathcal{P}} \equiv \widehat{\mathcal{P}}_+$, and write the Bose density matix

$$\rho_B(\boldsymbol{R}, \boldsymbol{R}'; \beta) = \frac{1}{N!}\sum_{\mathcal{P}}\rho_D(\boldsymbol{R}, \mathcal{P}\boldsymbol{R}'; \beta). \tag{2.18}$$

2.1.2 Bose-Einstein condensation

Bose-Einstein condensate is a state of matter in which the lowest energy level is macroscopically occupied, meaning the number of particles in the lowest level is of the order of the total number of particles N. This phenomenon does not occur in fermionic systems due to Pauli exclusion principle. We will show how this occurs in a uniform gas of non-interacting bosons.

The total number of particles must equal the sum of average occupation numbers of single-particle states, given by the Bose-Einstein (BE) distribution

$$N = \sum_i \bar{n}_i = \sum_i \frac{1}{e^{\beta(\epsilon_i - \mu)} - 1}, \tag{2.19}$$

ϵ_i being the energy of the state i, and μ the chemical potential. Normally, if N is large, and $k_B T$ is much greater than the difference in energy between levels, one can replace the sum in (2.19)

by an integral

$$N \approx N_T = \int \mathrm{d}\epsilon \, g(\epsilon) \frac{1}{e^{\beta(\epsilon_i - \mu)} - 1}, \tag{2.20}$$

where $g(\epsilon)$ is the density of states, and N_T is the number of excited particles, the thermal component of the system. We can equate the thermal component with the total number of particles because each state, including the ground state, is only microscopically occupied. However, if the ground state becomes macroscopically occupied it will not be accounted for in (2.20).

Due to the subtraction in the denominator of the BE distribution, and the fact that occupancy numbers can not be less than zero, there is a constraint on the chemical potential, namely $\mu \leq \epsilon_0$. It's value is fixed by the normalization condition

$$N = N_0 + N_T. \tag{2.21}$$

Bose-Einstein condensation (BEC) occurs in the limit $\mu \to \epsilon_0$, as the number of particles in the ground state $N_0 \equiv \bar{n}_0 = \{\exp[\beta(\epsilon_0 - \mu)] - 1\}^{-1}$ diverges. Certain conditions must be met in order for the transition to occur. The thermal component N_T is an increasing function of μ at a constant temperature. If its peak $N_c(T) = N_T(T, \mu = \epsilon)$ is greater than N, the system can not condense at that temperature. However, $N_c(T)$ decreases as temperature is lowered, and there may exist a temperature T_c at which it becomes equal to N. Below T_c, $N_0 = N - N_T$ is of the order of N, and $\mu \to \epsilon_0$ in the thermodynamic limit. To determine the critical temperature, we find the highest temperature at which N_0 is macroscopic by setting

$$N_T(T_c, \mu = \epsilon_0) = N \tag{2.22}$$

The density of states for a variety of systems is of the form [7]

$$g(\epsilon) = C_p \epsilon^{p-1}. \tag{2.23}$$

In case of a gas of free particles, $p = d/2$, where d is the dimensionality of the system. In a three dimensional system, we have a square-root dependence on energy, and $C_{3/2} = \frac{Vm^{3/2}}{2^{1/2}\pi^2\hbar^3}$. The ground-state has zero energy, so μ is always negative. Inserting (2.23) into (2.20)

$$N_T = C_p (k_B T)^p \, \Gamma(p) \, g_p\left(e^{\beta\mu}\right), \tag{2.24}$$

where

$$g_p(z) = \frac{1}{\Gamma(p)} \int_0^\infty \mathrm{d}x \, \frac{x^{p-1}}{z^{-1}e^x - 1} = \sum_{l=1}^{\infty} \frac{z^l}{l^p}. \tag{2.25}$$

Now we set $\mu = 1$, and insert (2.24) into (2.22) and obtain

$$k_B T_c = \left[\frac{N}{C_p \Gamma(p) g_p(1)} \right]^{1/p}. \tag{2.26}$$

Inserting $g_{3/2}(1) = 2.612$ for three-dimensional ideal gas, we have $k_B T \approx 3.31 \frac{\hbar^2 n^{2/3}}{m}$, where $n = N/V$ is the number density. On the other hand, for $p \leq 1$, $g_p(1)$ is divergent. It turns out that for $p = 1$ the equation (2.26) holds for $T_c = 0$, so in two dimensions, BEC occurs at zero temperature[5], but for $p < 1$, BEC does not occur at all.

Next we demonstrate the existence of off-diagonal long-range in the OBDM of a Bose-condensed system. We may write the momentum distribution as

$$n(\boldsymbol{p}) = \left\langle \hat{\boldsymbol{\Psi}}^\dagger(\boldsymbol{p}) \hat{\boldsymbol{\Psi}}(\boldsymbol{p}) \right\rangle. \tag{2.27}$$

Since $\hat{\boldsymbol{\Psi}}(\boldsymbol{p}) = (2\pi\hbar)^{-3/2} \int \mathrm{d}\boldsymbol{r} \exp(i\boldsymbol{p} \cdot \boldsymbol{r}/\hbar) \hat{\boldsymbol{\Psi}}(\boldsymbol{r})$, we have

$$n(\boldsymbol{p}) = \frac{1}{(2\pi\hbar)^3} \int \mathrm{d}\boldsymbol{r}\, \mathrm{d}\boldsymbol{r}'\, n(\boldsymbol{r}, \boldsymbol{r}') e^{i\boldsymbol{p}\cdot(\boldsymbol{r}-\boldsymbol{r}')/\hbar} \tag{2.28}$$

Assuming a uniform and isotropic system in a volume V, $n(\boldsymbol{r}, \boldsymbol{r}') = n(s = |\boldsymbol{r} - \boldsymbol{r}'|)$, and we can write

$$n(s) = \frac{1}{V} \int \mathrm{d}\boldsymbol{p}\, n(\boldsymbol{p}) e^{-i\boldsymbol{p}\cdot\boldsymbol{s}/\hbar}. \tag{2.29}$$

If $n(\boldsymbol{p})$ is a smooth function, the rapid oscillation of the exponential factor for large s will bring the OBDM to zero when $s \to \infty$. However, in presence of BEC, the momentum distribution has an $N_0 \delta(\boldsymbol{p})$ term, and this causes the OBDM to approach a finite value $n_0 = N/V$ for large s. This is referred to as the off-diagonal long-range order.

We will now identify the order parameter of the BEC transition starting with the field operator written in the form

$$\hat{\boldsymbol{\Psi}}(\boldsymbol{r}) = \phi_0(\boldsymbol{r}) \hat{a}_0 + \sum_{i \neq 0} \phi_i(\boldsymbol{r}) \hat{a}_i, \tag{2.30}$$

$\phi_i(\boldsymbol{r})$ and $\hat{a}_i$ being respectively the one-particle wave function and the annihilation operator corresponding to the i-th eigenstate of the OBDM. Since $\langle \hat{a}_0^\dagger \hat{a}_0 \rangle = N_0 \gg [\hat{a}_0, \hat{a}_0^\dagger] = 1$, we may replace the ladder operator in the first term on the right-hand side of (2.30) with $\sqrt{N_0}$. This way we treat the first, macroscopic term as a classical field $\boldsymbol{\Psi_0}(\boldsymbol{r})$, referred to as the wave function, and serving as the order parameter. This is called the Bogoliubov approximation. We may write $\boldsymbol{\Psi_0}$ in terms of its modulus and phase

$$\boldsymbol{\Psi_0}(\boldsymbol{r}) = |\boldsymbol{\Psi_0}(\boldsymbol{r}))|\, e^{iS(\boldsymbol{r})}. \tag{2.31}$$

[5]Note that this result is not valid for two-dimensional systems in general. For example, $p = 2$ in a harmonic trap, and T_c is finite.

The time dependent order parameter can be defined as

$$\mathbf{\Psi_0}(\boldsymbol{r}, t) = \mathbf{\Psi_0}(\boldsymbol{r}) e^{-i\mu t/\hbar}. \tag{2.32}$$

The time dependence is governed by the chemical potential because $\mathbf{\Psi_0}$ can be thought of as the matrix element of $\hat{\mathbf{\Psi}}$ between the ground states with N and $N+1$ particles, giving rise to the $E_{N+1} - E_N \approx \frac{\partial E}{\partial N} = \mu$ in the exponent [6, 7].

2.1.3 Superfluidity

Here we will describe the Landau's criterion for superfluidity. Essentially, the criterion is based on the possibility of energy dissipation through creation of energetically favourable elementary excitations in a fluid moving through a capillary.

First, we write the transformation laws of energy and momentum under Galilean transformations [6]

$$E' = E - \boldsymbol{P} \cdot \boldsymbol{V} + \frac{1}{2} M V^2, \tag{2.33}$$

$$\boldsymbol{P'} = \boldsymbol{P} - M\boldsymbol{V}, \tag{2.34}$$

where M is the total mass of the fluid, E and $\boldsymbol{P}$ are the energy and the momentum of the fluid in a reference frame K, and their primed counterparts are the energy and momentum in a different frame K', moving with velocity $\boldsymbol{V}$ relative to K.

Suppose an excitation with momentum $\boldsymbol{p}$ appears in a zero temperature uniform fluid flowing through a capillary at a constant velocity $\boldsymbol{v}$. The energy in the reference frame moving with the fluid is raised from ground state E_0 to $E_0 + \epsilon(\boldsymbol{p})$, $\epsilon(\boldsymbol{p})$ being the energy of the excitation, while the momentum becomes $\boldsymbol{p}$. According to (2.33) and (2.34), in the reference frame of the capillary, the energy and momentum are given by

$$E' = E_0 + \epsilon(\boldsymbol{p}) + \boldsymbol{p} \cdot \boldsymbol{v} + \frac{1}{2} M v^2 \tag{2.35}$$

$$\boldsymbol{P'} = \boldsymbol{p} + M\boldsymbol{v}. \tag{2.36}$$

The energy of the elementary excitation of momentum $\boldsymbol{p}$ in the frame moving with the capillary is given by $\epsilon(\boldsymbol{p}) + \boldsymbol{p} \cdot \boldsymbol{v}$. In order for excitations to spontaneously arise on account of relative motion, they have to reduce the total energy of the fluid from the perspective of the capillary, and therefore

$$\epsilon(\boldsymbol{p}) + \boldsymbol{p} \cdot \boldsymbol{v} < 0 \tag{2.37}$$

must hold. For momentum $\boldsymbol{p}$, this is possible if $v > \epsilon(\boldsymbol{p})/p$. We define the critical velocity v_c as the smallest velocity such that (2.37) can hold for any $\boldsymbol{p}$. Below v_c, the fluid is stable against

dissipation of its kinetic energy. Thus, the Landau's criterion for superfluidity is

$$v < v_c = \min_{\boldsymbol{p}} \frac{\epsilon(\boldsymbol{p})}{p}. \tag{2.38}$$

It depends on the shape of the excitation spectrum whether a system can achieve superfluidity, e.g. for the ideal Bose gas $\epsilon(\boldsymbol{p}) = \frac{p^2}{2m}$ leads to $v_c = 0$, while the weakly-interacting Bose gas, and even strongly-interacting $^4\mathrm{He}$ have a finite v_c [6].

At a finite temperature, small compared to the critical temperature for superfluidity, we may assume that our system is a gas of non-interacting quasiparticles corresponding to elementary excitations[6]. These quasiparticles can collide with the walls and exchange energy and momentum, but they only transport a part of the total mass, and the rest of the mass behaves like a superfluid. Therefore the system has superfluid and normal fluid components, and each has its own velocity, $\boldsymbol{v}_s$ and $\boldsymbol{v}_n$ respectively. In order for superfluidity to be possible, $|\boldsymbol{v}_s - \boldsymbol{v}_n| < v_c$ must hold. In equilibrium, the normal component must be at rest with respect to the capillary, therefore $v_n = 0$ in the frame of the capillary, and the relative velocity between the superfluid component, and the capillary is $\boldsymbol{v}_s - \boldsymbol{v}_n$. Now, we can use the energy of the excitation in the capillary frame to write the BE distribution function of quasiparticles

$$N_{\boldsymbol{p}} = \frac{1}{\exp\{\beta\left[\epsilon(\boldsymbol{p}) + \boldsymbol{p}\cdot(\boldsymbol{v}_s - \boldsymbol{v}_n)\right]\} - 1}. \tag{2.39}$$

It is of interest to determine the fraction of the system belonging to the superfluid component. As is shown in [6], the mass density of the normal component is given to the first order in $\boldsymbol{v}_s - \boldsymbol{v}_n$ by the Landau formula

$$\rho_n = -\frac{1}{3}\int \left.\frac{\mathrm{d}N_{\boldsymbol{p}}}{\mathrm{d}\epsilon}\right|_{\boldsymbol{v}_s-\boldsymbol{v}_n=0} (\epsilon)\, p^2 \frac{\mathrm{d}\boldsymbol{p}}{(2\pi\hbar)^3}. \tag{2.40}$$

The superfluid fraction can then be obtained from $\frac{\rho_s}{\rho} = 1 - \frac{\rho_n}{\rho}$. However, this theory is of limited applicability, since we have assumed, as mentioned, a uniform fluid at a low enough temperature, and well-defined, non-interacting elementary excitations.

A connection can be established between BEC and superfluidity by identifying the current density of the condensate with $n_0 v_s$, where $n_0 = |\Psi_0|^2$ is the number density of the condensate[7][6, 8]. The system is assumed here to be uniform, and $\boldsymbol{v}_s$ to be constant (or varying slowly enough). The current density is given by

$$\boldsymbol{j} = \frac{i\hbar}{2m}\left(\boldsymbol{\Psi_0}\boldsymbol{\nabla}\boldsymbol{\Psi_0^*} - \boldsymbol{\Psi_0^*}\boldsymbol{\nabla}\boldsymbol{\Psi_0}\right) = \frac{\hbar}{m} n_0 \boldsymbol{\nabla} S. \tag{2.41}$$

[6]This assumption is not always valid, e.g. in presence of disorder, elementary excitations are not well defined [6].

[7]However, it would be erroneous to assume that the density of the condensate is equal to the density of the superfluid.

Therefore,

$$\boldsymbol{v}_s = \frac{\hbar}{m}\boldsymbol{\nabla} S. \tag{2.42}$$

The phase S is the velocity potential, and it follows that the flow of superfluid is irrotational.

It should be noted that the connection we have established does not apply in the most general sense. Most notably, it breaks down in low dimensions. In two dimensions, irrotational superflow can exist in absence of off-diagonal long-range order at temperatures above absolute zero [6]. However the decay of the OBDM is algebraic instead of exponential in this case, indicating the existence of a quasi long-range order. Aside from this, superflow may be observed in systems of finite size, and as we will see, may be entirely a finite-size effect.

2.2 Path integral formalism

The path integral formalism, originating in the work of Richard P. Feynman, is a method that can be applied to study quantum systems. It is based on associating a probability amplitude with a completely specified motion of the system, its path. The integral over all possible paths within a region of space-time leads to the probability amplitude of the system occupying this region.

The formalism can be applied in slightly different manners to formulation of either quantum mechanics or quantum statistical mechanics. We will first briefly present the path integral formulation of quantum mechanics along the lines of Feynman's 1948. aritcle [2]. We will then turn to the path integral formulation of quantum statistical mechanics, which lays the theoretical foundation of the path integral Monte Carlo method.

2.2.1 Path integral formulation of quantum mechanics

This formulation of quantum mechanics rests on two postulates which we quote directly from [2]:

1. *If an ideal measurement is performed to determine whether a particle has a path lying in a region of space-time, then the probability that the result will be affirmative is the absolute square of a sum of complex contributions, one from each path in the region.*

2. *The paths contribute equally in magnitude, but the phase of their contribution is the classical action (in units of $\hbar$) ; i.e., the time integral of the Lagrangian taken along the path.*

We denote the space-time region of interest R. To understand what is meant by path lying in this region, we can imagine splitting the motion of a particle moving in the direction x in a large number of time slices t_i, separated by a time interval ϵ. The positions of the particle at

times t_i are denoted x_i. Letting $\epsilon \to 0$, the (x_i, t_i) pairs define the path $x(t)$. Region R can now be defined as a set of (a_i, b_i) pairs, and the paths lying in R satisfy $a_i < x_i < b_i$. We can now understand the concept of "ideal measurement" as a hypothetical measurement such that no further information may be extracted from it without disturbing the system beyond the disturbance of measuring weather the path lies in R. If a system was further disturbed, e.g. if one of the x_i's was collapsed into a specific value, the calculation of probability would have to change, since we would be dealing with classical probabilities instead of probability amplitudes.

The first postulate leads to the expression for probability amplitude of the path of the particle lying in a region R of space-time

$$\varphi(R) = \lim_{\epsilon \to 0} \int_R \Phi(..., x_i, x_{i+1}, ...) \cdots \mathrm{d}x_i \, \mathrm{d}x_{i+1} \cdots , \tag{2.43}$$

where the notation $\int_R$ stands for $\cdots \int_{a_i}^{b_i} \int_{a_{i+1}}^{b_{i+1}} \cdots$, and $\Phi(..., x_i, x_{i+1}, ...)$ is the complex contribution to the probability amplitude of a path defined by sequence of x_i's. As ϵ approaches zero, this essentially becomes a functional of path $\Phi[x(t)]$. The second postulate implies

$$\Phi[x(t)] \propto e^{\frac{i}{\hbar} S[x(t)]}, \tag{2.44}$$

S being the action, defined as the time integral of the classical Lagrangian along the path $x(t)$ $S[x(t)] = \int L(\dot{x}(t), x(t)) dt$. In order to pass (2.44) to (2.43), $x(t)$ has to be defined in the interval between t_i and t_{i+1}. This is done by assuming that the particle follows the classical path between t_i and t_{i+1}, that is the path of minimal action. We may write

$$S = \sum_i S(x_{i+1}, x_i), \tag{2.45}$$

and

$$S(x_{i+1}, x_i) = \min \int_{t_i}^{t_{i+1}} L(\dot{x}(t), x(t)) \, \mathrm{d}t \, . \tag{2.46}$$

Finally, we arrive at

$$\varphi(R) = \lim_{\epsilon \to 0} \int_R \exp\left[\frac{i}{\hbar} \sum_i S(x_{i+1}, x_i) \right] \prod_i \frac{\mathrm{d}x_i}{A}, \tag{2.47}$$

where $\prod_i 1/A$ is the normalization factor. This completes the path integral formulation of quantum mechanics.

In order to prove the equivalence of this formulation with ordinary quantum mechanics, we should be able to define the wave function, and show it obeys the Schrödinger's equation (this proof still neglects spin, however). We will cover this in a brief and somewhat crude manner,

and the reader may wish to see the full derivations in [2], or skip to the next section.

First we divide R into regions R' lying in the past, i.e. before some time $t' < t$ (t being the present), and R'' in the future, i.e. after some time $t'' > t$. The remaining region between t' and t'' can be arbitrarily narrow, and the values of the x coordinates are not restricted in this region. The value $|\varphi(R', R'')|^2$, if normalized by $|\varphi(R')|$, can be interpreted as the probability that if the system was in region R' it will later be found in region R''. We assign the index $i = 0$ to the present. The amplitude is given by

$$\varphi(R', R'') = \int \mathrm{d}x_0 \int\limits_{R''} \frac{1}{A} \prod_{i=0}^{\infty} \left\{ \exp\left[\frac{i}{\hbar} S(x_{i+1}, x_i)\right] \frac{\mathrm{d}x_{i+1}}{A} \right\} \int\limits_{R'} \prod_{i=-\infty}^{-1} \left\{ \exp\left[\frac{i}{\hbar} S(x_{i+1}, x_i)\right] \frac{\mathrm{d}x_i}{A} \right\} \tag{2.48}$$

Integration over the past and future regions R' and R'' in (2.48) produces functions $\psi(x_0, t)$ and $\chi^*(x_0, t)$ respectively

$$\varphi(R', R'') = \int \chi^*(x, t)\psi(x, t)dx. \tag{2.49}$$

The function $\psi(x, t)$ is dependent only on the past history of the system, and vice versa for $\chi^*(x, t)$. At time t, the entire information about the system is contained in $\psi(x, t)$. Future experiments can not distinguish between different histories, as long as they result in the same wave function. Similar remarks apply to $\chi^*(x, t)$ so it represents the complex conjugate of the wave function of a possible future state. We can interpret the right-hand side of (2.49) as the transition amplitude between the two states, i.e. the probability amplitude of a future measurement yielding the state χ if the system was prepared in state ψ.

A recursive relation, exact in the limit $\epsilon \to 0$, follows from the definition of $\psi(x, t)$

$$\psi(x_1, t + \epsilon) = \int\limits_{R} \exp\left[\frac{i}{\hbar} S(x_1, x_0)\right] \psi(x_0, t) \frac{\mathrm{d}x_0}{A}. \tag{2.50}$$

If we assume the relation is exact to the first order in ϵ, the accumulated error over a finite interval of time T will be of the order of $T\epsilon$, since the number of factors is T/ϵ, each carrying at most an error of order ϵ^2. Therefore the error will vanish in the limit $\epsilon \to 0$. We limit ourselves to a case of the Lagrangian being a quadratic function of velocities, without terms linear in velocity (i.e. the vector potential). The action can now be approximated as an integral over the path of a free particle[8]

$$S(x, x - \xi) = \frac{m\epsilon}{2} \left(\frac{\xi}{\epsilon}\right)^2 - \epsilon V(x), \tag{2.51}$$

[8]This is limited to rectangular coordinates

where $x = x_1$, $\xi = x_1 - x_0$, and $V(x)$ is the potential. Inserting this into (2.50), expanding the left-hand side to first order in ϵ, and $\psi(x-\xi)$ to second order of ξ we obtain

$$\begin{aligned}\psi(x,t) + \epsilon\frac{\partial\psi}{\partial t}(x,t) + ... = \\ = \exp\left[\frac{-i\epsilon V(x)}{\hbar}\right]\int \exp\left(\frac{im\xi^2}{2\hbar\epsilon}\right)\left[\psi(x,t) - \xi\frac{\partial\psi(x,t)}{\partial x} + \frac{\xi^2}{2}\frac{\partial^2\psi(x,t)}{\partial x^2} - ...\right]\frac{\mathrm{d}\xi}{A}.\end{aligned} \tag{2.52}$$

The only significant contribution to the right-hand side comes from region near $\xi = 0$, since otherwise the exponential due to kinetic action oscillates rapidly compared to variation in ψ when ϵ is small, and thus ensures cancellation. Upon integration, we find that agreement to zero order sets the value of A, and expanding the exponential due to potential action, we finally obtain the Schrödinger's equation for a particle in one dimension, accurate to the first order in ϵ

$$i\hbar\frac{\partial\psi}{\partial t} = -\frac{\hbar^2}{2m}\frac{\partial^2\psi}{\partial x^2} + V(x)\psi. \tag{2.53}$$

2.2.2 Path integrals in quantum statistical mechanics

If we rewrite the inverse temperature $\beta = u/\hbar$, the new variable u has the dimension of time, and will be referred to as "time" for reasons we hope will become clear soon. The density matrix now takes the form

$$\widehat{\rho}(u) = \exp\Big(-\frac{u}{\hbar}\widehat{H}\Big). \tag{2.54}$$

We note that we have switched to using an unnormalized form of the density matrix. We may break time up into M intervals of duration ϵ, and write

$$\widehat{\rho}(u = M\epsilon) = \Big[\exp\Big(-\frac{\epsilon}{\hbar}\widehat{H}\Big)\Big]^M. \tag{2.55}$$

If we write each of the factors i in (2.55) in the position representation $\rho(\boldsymbol{R}_i, \boldsymbol{R}_{i-1})$, integrate over $\boldsymbol{R}_i$ for all $i \neq 0, M$ we come to the rule of convolution

$$\rho(\boldsymbol{R}_M, \boldsymbol{R}_0; u) = \int \rho(\boldsymbol{R}_M, \boldsymbol{R}_{M-1}; \epsilon)\rho(\boldsymbol{R}_{M-1}, \boldsymbol{R}_{M-2}; \epsilon)\cdots\rho(\boldsymbol{R}_1, \boldsymbol{R}_0; \epsilon)\,\mathrm{d}\boldsymbol{R}_1\cdots\mathrm{d}\boldsymbol{R}_{M-1}\,. \tag{2.56}$$

Once again, when $\epsilon \to 0$, we have a path integral [1]

$$\rho(\boldsymbol{R}_M, \boldsymbol{R}_0; u) = \int \Phi[\boldsymbol{R}(s)]\,\mathscr{D}\boldsymbol{R}(s), \tag{2.57}$$

where $\mathscr{D}\boldsymbol{R}(u) = \lim\limits_{M\to\infty}\prod_{i=1}^{M-1}\frac{\mathrm{d}\boldsymbol{R}_i}{A}$.

In case of free particles, we simply insert (2.15) on the right-hand side of (2.56), and let

$\mathscr{D}\boldsymbol{R}(u)$ absorb the normalization constant[9] to find

$$\Phi[\boldsymbol{R}(s)] = \lim_{\epsilon\to 0}\exp\left\{-\frac{\hbar}{4\lambda}\sum_{i=0}^{M-1}\epsilon\left(\frac{\boldsymbol{R}_{i+1}-\boldsymbol{R}_i}{\epsilon}\right)^2\right\} = \exp\left\{-\frac{1}{\hbar}\int_0^u \frac{m}{2}\left[\dot{\boldsymbol{R}}(s)\right]^2 ds\right\}, \quad (2.58)$$

where we can recognize the kinetic energy term in the integral.

Since particles in a potential $V(\boldsymbol{R})$ become asymptotically free when ϵ is very small compared to the scale of significant variation of V, we can still use the density matrix of free particles (denoted ρ_0) for perturbation expansion of ρ

$$\rho(\boldsymbol{R},\boldsymbol{R}';\epsilon) = \rho_0(\boldsymbol{R},\boldsymbol{R}';\epsilon) + \delta\rho(\boldsymbol{R},\boldsymbol{R}';\epsilon), \quad (2.59)$$

where [1]

$$\delta\rho(\boldsymbol{R},\boldsymbol{R}';\epsilon) \approx -\int \mathrm{d}\boldsymbol{R}''\int_0^\epsilon \rho_0(\boldsymbol{R},\boldsymbol{R}'';\epsilon-u)V(\boldsymbol{R}'')\rho_0(\boldsymbol{R}'',\boldsymbol{R}';u)\frac{\mathrm{d}u}{\hbar}. \quad (2.60)$$

Due to small ϵ, the free density matrices are very localized, so the majority of contribution to the integral comes from the region in the vicinity of both $\boldsymbol{R}$, and $\boldsymbol{R}'$ (the $\boldsymbol{R}$ and $\boldsymbol{R}'$ have to be close in order for the integral to have a significant value). $V(\boldsymbol{R}'')$ can be taken to be constant in this region, and now the $\boldsymbol{R}''$ integral is simply a convolution of density matrices, so we find

$$\delta\rho(\boldsymbol{R},\boldsymbol{R}';\epsilon) \approx -\int \frac{\mathrm{d}u}{\hbar}V(\boldsymbol{R})\rho_0(\boldsymbol{R},\boldsymbol{R}';\epsilon) = -\frac{\epsilon}{\hbar}V(\boldsymbol{R})\rho_0(\boldsymbol{R},\boldsymbol{R}';\epsilon). \quad (2.61)$$

When dealing with larger ϵ the more accurate [1, 3] symmetrized form $\frac{\epsilon}{2\hbar}\left[V(\boldsymbol{R})+V(\boldsymbol{R}')\right]$ will be used. Equation (2.59) now becomes

$$\begin{aligned}\rho(\boldsymbol{R},\boldsymbol{R}';\epsilon) &\approx \rho_0(\boldsymbol{R},\boldsymbol{R}';\epsilon)\left[1-\frac{V(\boldsymbol{R})}{\hbar}\epsilon\right]\\ &\approx \left(\frac{4\pi\lambda\epsilon}{\hbar}\right)^{-3N/2}\exp\left\{-\epsilon\left[\frac{\hbar}{4\lambda}\left(\frac{\boldsymbol{R}-\boldsymbol{R}'}{\epsilon}\right)^2+\frac{V(\boldsymbol{R})}{\hbar}\right]\right\}.\end{aligned} \quad (2.62)$$

This amounts to the primitive approximation in which the commutator terms of the order higher than ϵ are ignored in the Baker-Campbell-Hausdorff formula

$$\exp\left[-\frac{\epsilon}{\hbar}(\widehat{\mathcal{T}}+\widehat{\mathcal{V}})+\frac{\epsilon^2}{2\hbar^2}[\widehat{\mathcal{T}},\widehat{\mathcal{V}}]+\ldots\right] = \exp\Big(-\frac{\epsilon}{\hbar}\widehat{\mathcal{T}}\Big)\exp\Big(-\frac{\epsilon}{\hbar}\widehat{\mathcal{V}}\Big). \quad (2.63)$$

The primitive approximation becomes exact in the sense that the error does not accumulate

[9] This is done for mathematical convenience, and we will reintroduce the normalization when dealing with discrete paths.

when $\epsilon \to 0$[3]. Finally,

$$\rho(\boldsymbol{R}_M, \boldsymbol{R}_0; u) = \int \exp\left\{ -\frac{1}{\hbar} \int_0^u \left[\frac{m}{2} \dot{\boldsymbol{R}}(s)^2 + V\left(\boldsymbol{R}(s)\right) \right] \mathrm{d}s \right\} \mathscr{D}\boldsymbol{R}(s) \tag{2.64}$$

Note the similarity between equations (2.62) and (2.51). If we define

$$S^i \equiv S(\boldsymbol{R}_i, \boldsymbol{R}_{i-1}; \epsilon) \equiv -\hbar \ln[\rho(\boldsymbol{R}_i, \boldsymbol{R}_{i-1}; \epsilon)], \tag{2.65}$$

then $S^i = K^i + U^i$, where the kinetic action is

$$K^i = \frac{3N\hbar}{2} \ln\left(\frac{4\pi\lambda\epsilon}{\hbar}\right) + \frac{\hbar^2}{4\lambda} \frac{(\boldsymbol{R}_i - \boldsymbol{R}_{i-1})^2}{\epsilon}, \tag{2.66}$$

and the potential action is simply the difference between the total and kinetic action. In primitive approximation, the potential action is written

$$U_1^i = \frac{\epsilon}{2} \left[V(\boldsymbol{R}_i) + V(\boldsymbol{R}_{i-1}) \right], \tag{2.67}$$

where we have used the more precise symmetrized form as noted earlier, and the index represents the order of approximation in ϵ. We return now to the equation (2.56) and rewrite it as

$$\rho(\boldsymbol{R}_M, \boldsymbol{R}_0; u) = \int \exp\left[-\frac{1}{\hbar} \sum_{i=1}^{M} S(\boldsymbol{R}_i, \boldsymbol{R}_{i-1}; \epsilon) \right] \prod_{i=1}^{M-1} \mathrm{d}\boldsymbol{R}_i \tag{2.68}$$

Again, we see a striking similarity to an earlier result from path integral quantum mechanics, the probability amplitude of a path lying in space-time region R (2.47), and we can see how the variable $u \propto T^{-1}$ plays a role similar to conventional time. However, the imaginary unit is lacking in the exponent of (2.68). We can introduce it by switching to imaginary time $t = \frac{u}{i}$ and $\epsilon \to i\epsilon$ [5]. For the sake of argument, we ignore the constant term on the right-hand side of (2.66), letting it be absorbed by $\mathscr{D}\boldsymbol{R}(s)$ as before. Then the two equations are identical in form, and it can readily be shown that the kinetic and potential parts of action have different signs, as it should be the case, since the action is conventionally defined as the time integral of the Lagrangian. Now the density matrix element in coordinate representation can be interpreted as the probability amplitude for a system of N particles to travel from $\boldsymbol{R}_0$ to $\boldsymbol{R}_M$ in duration $t = \frac{\beta}{i\hbar}$ of imaginary time [1]. The amplitude is obtained by summing up contributions from all possible paths. This interpretation implies the possibility of numerical calculation of the density matrix by sampling random walks.

Classical isomorphism

We will now discuss the isomorphism between quantum and certain classical statistical systems [3], and use this opportunity to introduce some terminology along the way. Expression (2.68) is also equivalent in form to a configuration integral of a classical system at an inverse temperature of $\tau = \epsilon/\hbar = \beta/M$, as can be seen by extracting ϵ from the action. It is important not to confuse the temperature of the classical system with the temperature of the quantum system defined by β[10]. The system in question is composed of N chains of particles, referred to as *beads* to avoid confusion with the physical particles. These chains are called *polymers*, and each represents a path of a particle in imaginary time, or its *world line*. The m-th bead in each polymer corresponds to one of the N particles at the discrete point in time $u_m = m\epsilon$. A vector $\boldsymbol{R}_m = \{\boldsymbol{r}_{1,m}, ..., \boldsymbol{r}_{N,m}\}$ will be referred to as the m-th *time slice*, since it contains the configuration of the system at the time u_m. A pair of successive time slices $(\boldsymbol{R}_{m-1}, \boldsymbol{R}_m)$ is the *link* m, and the action S^m, as defined in (2.65), is the action of the link m.

The action divided by ϵ plays the role of the potential energy. Examining this potential energy function, we see that the kinetic part of the action gives rise to the spring potential between the successive beads of the same polymer, and the potential action plays the same role of potential between different particles. Note that this results in a rather peculiar classical system in which the beads belonging to different polymers only interact if they are at the same time slice.

We are especially interested in diagonal elements of the density matrix $\rho(\boldsymbol{R}_0, \boldsymbol{R}_M = \boldsymbol{R}_0)$. In fact, it makes sense to view the time u as periodic with period $\beta\hbar$. Now the polymers become *ring polymers*. Due to quantum-classical isomorphism, any property that can be written in terms of the partition function, or even the density matrix elements, has an analogue in the statistical mechanics of classical ring polymers [3]. Two ring polymers are schematically presented in Figure 2.1

Of course, the picture we have just presented only applies to distinguishable particles. As we have seen earlier, the Bose density matrix and partition function must include a sum over all possible permutations

$$Z_B = \frac{1}{N!}\sum_{\mathcal{P}}\int \rho(\boldsymbol{R}_0, \mathcal{P}\boldsymbol{R}_M = \boldsymbol{R}_0; \beta)\,\mathrm{d}\boldsymbol{R}_0 = \frac{1}{N!}\int \exp\left[-\frac{1}{\hbar}\sum_{m=1}^{M} S^m\right]\prod_{m=0}^{M-1}\mathrm{d}\boldsymbol{R}_m \quad (2.69)$$

The boundary condition $\mathcal{P}\boldsymbol{R}_M = \boldsymbol{R}_0$ implies that the polymers can become "cross-linked", since the polymer that contains the $\boldsymbol{r}_{i,0}$ bead can close onto $\boldsymbol{r}_{j,0}$, where $j = \mathcal{P}_i$, after one time period β. Since any permutation is a product of cyclic permutations, the chain will eventually close onto $\boldsymbol{r}_{i,0}$ again. Multiple ring polymers are thus connected into one, and in presence of non-identity permutations, the number of rings is reduced by $n-1$ for every n-cycle. The

[10] In fact, it makes sense in application to keep the time interval constant as quantum temperature is changed

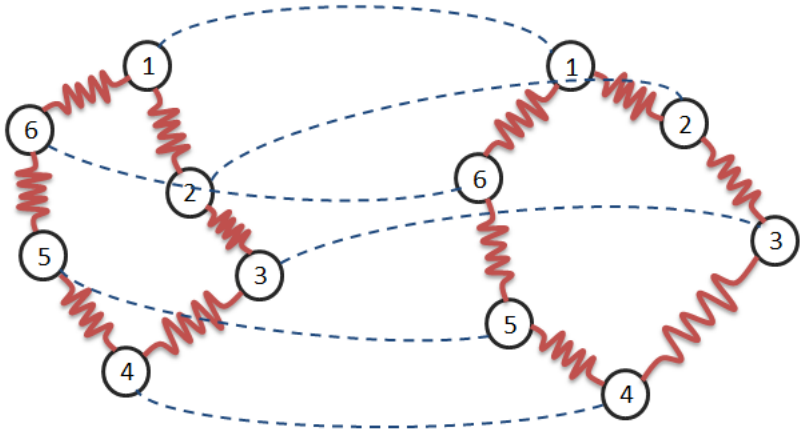

Figure 2.1: *The figure is a schematic representation of two ring polymers. The successive beads in the same polymer are connected by "springs", and the beads belonging to the same time slice by dashed lines. The image is reproduced with permission from [29].*

relative probabilities of various permutations are controlled by action in the same manner as before. In absence of interactions, the size of a polymer is of the order of thermal wavelength. Therefore, at high temperatures, distance between polymers will tend to be much larger than their size, and the dominant permutation will be the identity, since any exchange would require large lengthening of the springs. On the other hand, thermal wavelength is infinite at zero temperature, and space is completely filled with beads, so every permutation is equally likely. We may define the degeneracy temperature, at which the exchange effects become important, by setting the thermal wavelength equal to the typical interparticle spacing $\rho^{-1/3}$

$$k_B T_D = \frac{\hbar^2 \rho^{2/3}}{m}. \tag{2.70}$$

When enough polymers become connected, the resulting polymer may become macroscopic. It is the appearance of macroscopic polymers that indicates the superfluid transition [3]. In finite-size systems with periodic boundary conditions, the paths may wind around the container by crossing the boundary, and eventually reconnecting with a periodic image of its initial point. This is analogous in nature to formation of macroscopic polymers, and we explain the relation of winding to superfluidity in the next section.

2.2.3 Path winding and superfluidity

The fraction of superfluid can be determined by examining the response of the free energy of a system to the movement of the boundary [14]. A usual example is a system between by two cylinders of radii R and $R + \delta$, rotating with angular frequency ω. For $\delta/R \ll 1$, the system

becomes essentially equivalent to a $2\pi R$-periodic system enclosed by two planes moving with velocity $v = R\omega$. Here we study a more general system enclosed in a d-dimensional box, periodic in at least one direction, in a manner similar to [14].

Let $\widehat{\rho}_{\boldsymbol{v}}$ be the density matrix of a system with walls moving with an arbitrary velocity $\boldsymbol{v}$. Since the distribution is identical in the lab and moving frame, we have $\widehat{\rho}_{\boldsymbol{v}} = \widehat{\rho}' = e^{-\beta \widehat{H}'}$, where primed frame is at rest with the boundary, and

$$\widehat{H}' = \sum_{i=1}^{N} \frac{(-i\hbar \boldsymbol{\nabla}_i - m\boldsymbol{v})^2}{2m} + V(\boldsymbol{R}). \tag{2.71}$$

We can define the normal component as the part which responds to the boundary motion. This implies

$$\frac{\rho_n}{\rho} N m \boldsymbol{v} = \langle \widehat{P} \rangle_{\boldsymbol{v}} = \frac{\operatorname{Tr} \widehat{\rho}_{\boldsymbol{v}} \widehat{P}}{\operatorname{Tr} \widehat{\rho}_{\boldsymbol{v}}}, \tag{2.72}$$

which we may rewrite as

$$\frac{\rho_n}{\rho} N m \boldsymbol{v} = \frac{1}{\beta} \boldsymbol{\nabla}_{\boldsymbol{v}} \ln(\operatorname{Tr} \widehat{\rho}_{\boldsymbol{v}}) + N m \boldsymbol{v}. \tag{2.73}$$

Since $e^{-\beta F_{\boldsymbol{v}}} = \operatorname{Tr} \widehat{\rho}_{\boldsymbol{v}}$, and $\frac{\rho_S}{\rho} = 1 - \frac{\rho_N}{\rho}$, by applying the chain rule we obtain

$$\frac{\rho_S}{\rho} = \frac{\partial F_{\boldsymbol{v}}}{\partial (\frac{1}{2} m v^2)}. \tag{2.74}$$

Integrating form zero velocity to $\boldsymbol{v}$, and expanding around constant fraction, we obtain the connection between the free energy response due to boundary motion and the fraction of superfluid

$$\frac{\Delta F_{\boldsymbol{v}}}{N} = \frac{1}{2} m v^2 \, \frac{\rho_S}{\rho} + \mathcal{O}(v^4). \tag{2.75}$$

As expected, due to dissipation, there is little impact of boundary motion on the bulk of the normal fluid. However, the free energy response is proportional to the superfluid fraction.

From (2.12), we know that

$$-\frac{\partial \rho_{\boldsymbol{v}}(\boldsymbol{R}, \boldsymbol{R}^*; \beta)}{\partial \beta} = \widehat{H}' \rho_{\boldsymbol{v}}(\boldsymbol{R}, \boldsymbol{R}^*; \beta), \tag{2.76}$$

with boundary condition

$$\rho_{\boldsymbol{v}}(\boldsymbol{R}, \{\boldsymbol{r}_1^*, \ldots, \boldsymbol{r}_j^* + \boldsymbol{L}, \ldots, \boldsymbol{r}_n^*\}; \beta) = \rho_{\boldsymbol{v}}(\boldsymbol{R}, \boldsymbol{R}^*; \beta). \tag{2.77}$$

We can write

$$e^{-\beta \Delta F_{\boldsymbol{v}}} = \frac{\int \rho_{\boldsymbol{v}}(\boldsymbol{R}, \boldsymbol{R}; \beta) \, \mathrm{d}\boldsymbol{R}}{\int \rho_{\boldsymbol{v}=\boldsymbol{0}}(\boldsymbol{R}, \boldsymbol{R}; \beta) \, \mathrm{d}\boldsymbol{R}}, \tag{2.78}$$

where $\rho_{\boldsymbol{v}=\boldsymbol{0}}$ is the solution of the equation of motion for stationary walls. It can be shown by inserting in (2.76) that this equation is satisfied by $\tilde{\rho}$, defined by

$$\rho_{\boldsymbol{v}}(\boldsymbol{R}, \boldsymbol{R}^*; \beta) = \exp\left[i\frac{m}{\hbar}\boldsymbol{v} \cdot \sum_i (\boldsymbol{r}_i - \boldsymbol{r}_i^*)\right] \tilde{\rho}(\boldsymbol{R}, \boldsymbol{R}^*; \beta). \tag{2.79}$$

Obviously, we have $e^{-\beta F_{\boldsymbol{v}=\boldsymbol{0}}} = \operatorname{Tr} \tilde{\rho}$, which is precisely the denominator of (2.78), but one thing remains to be clarified. Setting $\boldsymbol{R}^* = \boldsymbol{R}$, the sum in the exponent of (2.79) takes the form

$$\sum_i (\boldsymbol{r}_{\mathcal{P}i} - \boldsymbol{r}_i) \equiv \boldsymbol{W}, \tag{2.80}$$

where the *winding vector* $\boldsymbol{W}$ counts the number of times the paths wind around the box in each direction. Its components W_α are quantized in units of L_α, the length of the box in the α direction. If the path closes onto the k-th periodic image of the initial bead, then $W_\alpha = kL_\alpha$. Now we may write

$$e^{-\beta \Delta F_{\boldsymbol{v}}} = \frac{\int e^{i\frac{m}{\hbar}\boldsymbol{v}\cdot\boldsymbol{W}} \tilde{\rho}(\boldsymbol{R}, \boldsymbol{R}; \beta)\, \mathrm{d}\boldsymbol{R}}{\int \tilde{\rho}(\boldsymbol{R}, \boldsymbol{R}; \beta)\, \mathrm{d}\boldsymbol{R}} = \left\langle e^{i\frac{m}{\hbar}\boldsymbol{v}\cdot\boldsymbol{W}} \right\rangle. \tag{2.81}$$

Since velocity is arbitrary, we may take it to be small. All of the odd terms in the expansion of $e^{i\frac{\hbar}{2\lambda}\boldsymbol{v}\cdot\boldsymbol{W}}$ average to zero, and we have

$$\beta \Delta F_{\boldsymbol{v}} = \frac{m^2}{2\hbar^2} \left\langle (\boldsymbol{v} \cdot \boldsymbol{W})^2 \right\rangle + \mathcal{O}(v^4) = \frac{m^2 v^2}{2\hbar^2} \left\langle W^2 \right\rangle + \mathcal{O}(v^4), \tag{2.82}$$

where $W = \frac{\boldsymbol{v}}{|\boldsymbol{v}|} \cdot \boldsymbol{W}$ is the *winding number* in the direction of $\boldsymbol{v}$. If we take $\boldsymbol{v} = v_x \hat{\boldsymbol{e}}_x$ for example, it is the x component of the winding vector, and if our box is a d-dimensional hypercube, it becomes obvious due to symmetry that $\langle W^2 \rangle = \frac{1}{d} \langle \boldsymbol{W}^2 \rangle$. By comparing (2.82) with (2.75), we finally arrive at the expression for the superfluid fraction in terms of the mean square winding number, which can be calculated from the flux of paths across any plane

$$\frac{\rho_S}{\rho} = \frac{\langle W^2 \rangle}{2\lambda\beta N}. \tag{2.83}$$

2.3 One-dimensional systems

Next, we turn to the theory of quantum one-dimensional systems. 1D systems are fundamentally different from their higher-dimensional counterparts which causes many of the methods developed for studying 3D systems to fail. Before moving on to the Luttinger liquid theory that is of particular interest for this thesis, we will briefly mention some of the important results. Recall that BEC does not exist in 1D. This is due to the fact that fluctuations of the phase destroy long-range order. Even algebraic order is only present at zero temperature [6]. We will see

that superflow can exist in 1D, but only in systems confined to small size, since imaginary-time paths are still able to wind around the system in presence of periodic boundary conditions.

2.3.1 Theory of Luttinger liquids

The Tomonaga-Luttinger model is a theory developed for studying the low energy properties of 1D systems of interacting fermions. We will use the term *Luttinger liquid* (LL) to refer to either this model or any systems that share its low energy characteristics, which includes a variety of 1D systems, not necessarily fermionic. The LL model is an analogue of the Fermi liquid model which fails in 1D. The Fermi liquid is a generalization of the Fermi gas to systems of interacting fermions, and it preserves a lot of the properties of the Fermi gas, notably the discontinuity of the zero-temperature fermion distribution at the Fermi surface[11], and the excitations that have a one-to-one correspondence to the free system. Near the Fermi surface, the excitations resemble particle-hole pairs, but have a finite lifetime, which can nevertheless be considered infinitely long for most practical purposes [9, 10].

The LL model describes the low lying excitations around the two Fermi points[12]. As long as we stay in the vicinity of Fermi points, the dispersion relation can be linearized, leading to Hamiltonian [10]

$$\widehat{H} = \sum_{\alpha=\pm1} v_F \int \mathrm{d}x\, \hat{\mathbf{\Psi}}^\dagger_\alpha (i\hbar\alpha\partial_x - \hbar k_F)\hat{\mathbf{\Psi}}_\alpha - \frac{1}{2}\int \mathrm{d}x\, \mathrm{d}x'\, \rho(x)V(x-x')\rho(x'), \tag{2.84}$$

where α labels the Fermi points, and v_F and $\hbar k_F$ are Fermi velocity and momentum. The $\pm$ fields correspond to excitations moving in opposite directions, and the density is given by $\widehat{\rho} = \hat{\mathbf{\Psi}}^\dagger_+\hat{\mathbf{\Psi}}_+ + \hat{\mathbf{\Psi}}^\dagger_-\hat{\mathbf{\Psi}}_-$. Various methods can be applied to this model, including perturbation theory, renormalization groups, and bosonization. The last is of most interest to us since it is specific to 1D, and makes obvious the connection to Bose systems in 1D.

Let us start from a Bose fluid of average density $\rho_0 = N_0/L$, and let $\hat{\mathbf{\Psi}}(x)$ be an L-periodic field satisfying the commutation relation

$$[\hat{\mathbf{\Psi}}(x), \hat{\mathbf{\Psi}}^\dagger(x')] = \delta(x-x'). \tag{2.85}$$

The Hamiltonian of the fluid is given by

$$\widehat{H} = \frac{\hbar^2}{2m}\int \mathrm{d}x\, |\boldsymbol{\nabla}\hat{\mathbf{\Psi}}|^2 + \frac{1}{2}\int \mathrm{d}x\, \mathrm{d}x'\, \hat{\mathbf{\Psi}}^\dagger(x)\hat{\mathbf{\Psi}}^\dagger(x')V(x-x')\hat{\mathbf{\Psi}}(x)\hat{\mathbf{\Psi}}(x'). \tag{2.86}$$

[11] Note that the magnitude of the jump is decreased since the distribution is no longer a step function.
[12] The analogue of the Fermi surface in 1D.

We proceed by introducing the phase-density representation

$$\hat{\mathbf{\Psi}}^\dagger(x) = \sqrt{\widehat{\rho}(x)}e^{i\widehat{\varphi}(x)}, \tag{2.87}$$

where

$$\widehat{\rho}(x) = \sum_{n=1}^{N} \delta(x - x_n) \tag{2.88}$$

is the density operator, and $\widehat{\varphi}$ the phase operator. Then, assuming $e^{i\widehat{\varphi}}$ commutes with itself for $x \neq x'$, it follows from commutator (2.85) that

$$[\widehat{\rho}(x), e^{i\widehat{\varphi}(x')}] = e^{i\widehat{\varphi}(x)}\delta(x - x'), \tag{2.89}$$

By averaging the density over lengths much larger than ρ_0^{-1} we obtain the smeared density

$$\widehat{\rho}_s(x) = \rho_0 + \widehat{\Pi}(x), \tag{2.90}$$

where $\widehat{\Pi}(x)$ is a local fluctuation field representing the long-wavelength zero-point fluctuations which dominate low-energy properties[11]. We may treat $\widehat{\Pi}(x)$ and $\widehat{\varphi}(x)$ as conjugate variables, so that

$$[\widehat{\varphi}(x), \widehat{\rho}_s(x')] = [\widehat{\varphi}(x), \widehat{\Pi}(x')] = i\delta(x - x'), \tag{2.91}$$

since this is compatible with (2.89), but we stress that it is not compatible with the definition (2.88) of the density operator. (2.91) only holds for the smeared density which ignores (i.e. averages over) all the physics below the ρ_0^{-1} length scale.

From here, we may construct a representation of the unsmeared density operator that preserves its discreteness. We introduce a new field $\widehat{\theta}(x)$ that satisfies $\boldsymbol{\nabla}\widehat{\theta}(x) = \pi[\rho_0 + \widehat{\Pi}(x)]$, and the boundary condition $\widehat{\theta}(x + L) = \widehat{\theta}(x) + \pi N$. The boundary condition is consistent with the periodicity of density, and implies that the field increases by πN when moving right from 0 to L. It is natural to take the field as monotonically increasing, and to identify the positions x_i, where $\widehat{\theta}(x)$ is a multiple of π, with the positions of particles. It is worth mentioning that a similar boundary condition has to apply to the phase field $\widehat{\varphi}(x + L) = \widehat{\varphi}(x) + \pi J$, where J is an even integer. Non-zero J implies a topologically excited state of the phase field corresponding to total current [10]. The two fields satisfy a commutation relation $[\widehat{\varphi}(x), \widehat{\theta}(x')] = \frac{i\pi}{2}\,\mathrm{sgn}\,(x - x')$ Finally, using the composition property of the Dirac delta function $\delta(f(x)) = \sum_i \frac{\delta(x-x_i)}{|f'(x_i)|}$ [13], we rewrite (2.88) as[14]

$$\widehat{\rho}(x) = \boldsymbol{\nabla}\widehat{\theta}(x) \sum_{i=1}^{N} \delta(\widehat{\theta}(x) - n\pi) = [\rho_0 + \widehat{\Pi}(x)] \sum_{m=-\infty}^{+\infty} e^{i2m\widehat{\theta}(x)}. \tag{2.92}$$

[13] The summation goes over roots of $f(x)$, and it is assumed all roots are simple.

[14] The last equality is obtained by using the Poisson summation formula.

This is the Haldane's ansatz. The last expression is an expansion, and it is often enough to keep only a few terms, since high order terms oscillate rapidly and disappear when averaging over progressively shorter distances. Keeping only the $m = 0$ term, we would arrive back at the smeared density.

We may now rewrite the field creation operator for bosons by inserting (2.92) in (2.87)

$$\hat{\mathbf{\Psi}}_B^\dagger(x) = A\sqrt{\rho_0 + \widehat{\Pi}(x)} \sum_m e^{i2m\widehat{\theta}(x)} e^{i\widehat{\varphi}(x)}, \tag{2.93}$$

where A is an undetermined normalization constant, dependent on the high energy properties, that stems from the fact that the square root of a delta function is also a delta function up to a normalization factor. We may have done a similar procedure for a Fermi field. The crucial difference is that the Fermi field operators satisfy an anticommutator equation analogous to (2.85). We can immediately derive the expression for such Fermi field by simply multiplying the Bose field by factor $e^{i\widehat{\theta}(x)}$, which amounts to shifting $2m \to 2m+1$ in the exponent[15]. Note that this modifies the selection rule on the topological quantum number J, so that $J + N$ must be even for fermions. The difference reflects the fact that a particle can be added to a $k = 0$ state in a Bose system without creating any current, while this is impossible in a Fermi system.

Having introduced the $\widehat{\theta}$ and $\widehat{\varphi}$, we can write the Hamiltonian in terms of these fields. By expanding (2.86) to second order around constant density and zero current we obtain a harmonic form as in [11]

$$\widehat{H} = \frac{\hbar}{2\pi} \int \mathrm{d}x \left[v_J (\boldsymbol{\nabla}\widehat{\varphi})^2 + v_N (\boldsymbol{\nabla}\widehat{\theta} - \pi\rho_0)^2 \right], \tag{2.94}$$

where in a Galilean invariant system

$$v_J = v_J^0 = \frac{\pi\hbar\rho_0}{m}, \tag{2.95}$$

and $v_N = (\pi\hbar\rho_0^2)^{-1}\kappa$ depends on compressibility (κ) which includes the effects of short-wavelength physics. These two parameters determine the low-energy properties of the system.

It is of interest for this thesis to find the asymptotic $x \gg \rho_0^{-1}$ behaviour of certain correlation functions for systems in LL regime, namely the density-density function and the boson OBDM. The results derived in [11] at zero temperature using the model presented above are

$$\rho_0^2 g(x) = \langle \widehat{\rho}(x)\widehat{\rho}(0)\rangle = \rho_0^2 \left[1 - \frac{2K}{(2\pi\rho_0 x)^2} + \sum_{m=1}^{\infty} A_m (\rho_0 x)^{-2m^2 K} \cos(2\pi m \rho_0 x) \right], \tag{2.96}$$

$$\rho(x,0) = \left\langle \hat{\mathbf{\Psi}}_B^\dagger(x) \hat{\mathbf{\Psi}}_B(0) \right\rangle = \rho_0 (\rho_0 x)^{-\frac{1}{2K}} \sum_{m=0}^{\infty} B_m (\rho_0 x)^{-2m^2 K} \cos(2\pi m \rho_0 x). \tag{2.97}$$

[15]The (anti)commutator equations are not perfectly satisfied in this representation, but the additional terms come with oscillating factors which can be ignored for the purpose of a low-energy description[10].

The A_m and B_m are parameters depending on the short-wavelength structure, and $K = \sqrt{\frac{v_J}{v_N}}$ is the so-called Luttinger parameter.

Winding paths essentially represent imaginary time currents and the LL model makes a prediction about the distribution of the winding number [15]

$$P(W) = \frac{e^{-\frac{\pi L}{2\hbar\beta v_J}W^2}}{\sum\limits_{W'=-\infty}^{+\infty} e^{-\frac{\pi L}{2\hbar\beta v_J}W'^2}} = \frac{e^{-\frac{\pi L}{2\hbar\beta v_J}W^2}}{\vartheta_3\left(0, e^{-\frac{\pi L}{2\hbar\beta v_J}}\right)}, \tag{2.98}$$

where the winding number can take values $W = 0, \pm 1, \ldots$ [16], and $\vartheta_3(z,q) = \sum\limits_{n=-\infty}^{+\infty} q^{n^2} e^{2niz}$ is the Jacobi Theta function of the third kind. Knowing the distribution of the winding paths, it is possible to evaluate its mean square, and by (2.83), the LL prediction for the superfluid fraction [17]

$$\frac{\rho_S}{\rho} = \frac{mL^2}{\hbar^2\beta N}\sum_{W=-\infty}^{+\infty} W^2 \frac{e^{-\frac{\pi L}{2\hbar\beta v_J}W^2}}{\vartheta_3\left(0, e^{-\frac{\pi L}{2\hbar\beta v_J}}\right)} = \frac{\pi L}{4\hbar\beta v_J^0}\left|\frac{\vartheta_3''(0, e^{-\frac{\pi L}{2\hbar\beta v_J}})}{\vartheta_3(0, e^{-\frac{\pi L}{2\hbar\beta v_J}})}\right|. \tag{2.99}$$

We see that the superfluid density can be expressed as a function of a single scaling variable $u = \frac{L}{\hbar\beta v_J}$,

$$\frac{\rho_S}{\rho} = \frac{\pi}{4}u_0\left|\frac{\vartheta_3''(0, e^{-\frac{\pi}{2}u})}{\vartheta_3(0, e^{-\frac{\pi}{2}u})}\right|, \tag{2.100}$$

where $u_0 = \frac{L}{\hbar\beta v_J^0}$. We stress the fact that the only temperature or L dependence of ρ_S/ρ is through $u \propto LT$, and not individually. At finite temperature, ρ_S/ρ invariably goes to zero in the thermodynamic limit, in accordance with the expected absence of phase transition at finite temperature in 1D. In a Galilean invariant system, one can equivalently write

$$\frac{\rho_S}{\rho} = 1 - \frac{\pi}{u}\left|\frac{\vartheta_3''(0, e^{-\frac{2\pi}{u}})}{\vartheta_3(0, e^{-\frac{2\pi}{u}})}\right|, \tag{2.101}$$

with $u = u_0$. We will use (2.100) and (2.101) to test the applicability of the LL results to 1D systems under various conditions.

[16] Note that the winding number is no longer defined as quantized in units of L,

Chapter 3

Methods

We have used the tool of computational simulation to obtain predictions about the behaviour of physical systems differing in characteristics such as temperature and density. The simulation approach allows us to set up a system and derive predictions by observing its simulated behaviour, which reduces the need for ever more simplified theoretical models and assumptions. In this way, the computational method complements purely theoretical methods, allowing us to compare results, and test the limits of applicability of theoretical models. However, the simulation method introduces its own challenges and uncertainties. Since approximations have to be made, there is a question of precision of results. The appropriate numerical methods have to be chosen so that the resulting distributions converge towards the desired ones, or that the system trajectories do not accumulate error and diverge from exact solutions of the equations of motion, etc. Care should be taken to allow large systems to achieve equilibrium before collecting results if there is possibility that initial configurations will significantly affect results.

In this chapter, we provide insight into the methods that were used. First, we describe the basic process and its intended results. Then we lay out the most important aspects of the computational method used to perform simulations.

3.1 Physical model and the basic simulation procedure

The method behind our simulations is called Path integral Monte Carlo (PIMC). It is a stochastic method that uses the ideas presented in section 2.2.2. The systems we investigate are composed of a relatively small predefined number of bosons, between 3 and 20 contained in a 1D box with periodic boundary condition. The length of the box L is also predefined, along with the temperature, so our systems are described by the canonical ensemble. Even though periodic images of particles make the system infinite in a sense, it is still necessary in theory to take the thermodynamic limit to eliminate finite-size effects, since phenomena on large scales cannot be

accounted for, and wave-like phenomena become quantized. The size of our simulated systems was not nearly enough to eliminate all finite-size effects, and in fact, they play a central role in the matter studied in this thesis, namely, superflow in 1D systems is a finite-size effect.

The bosons in our simulations, which we refer to as atoms, are defined by their mass, initial position, and mutual interaction. The mass corresponds to the mass of $^4\mathrm{He}$ ($\lambda \approx 6.06\,\text{Å}^2\,\text{K}$), or in some cases $^3\mathrm{He}$ ($\lambda = 8.08\,\text{Å}^2\,\text{K}$). We use these to refer to the species of the atoms, but note that it is not our aim here to study any specific system, but obtain some general predictions that can either be applied to some specific systems or motivate and direct further research. This explains why we may take atoms of mass equal to that of $^3\mathrm{He}$ to be bosons – our system need not be realistic. The interaction potential used is the Lennard-Jones (LJ) potential

$$V(r) = 4\varepsilon\left[\left(\frac{\sigma}{r}\right)^{12} - \left(\frac{\sigma}{r}\right)^{6}\right], \tag{3.1}$$

with values of parameters $\varepsilon = 10.22\,\text{K}$, and $\sigma = 2.556\,\text{Å}$. The precise potential used is probably not very important, since low-energy properties of dilute systems[1] are mostly dependent on the scattering length of the potential [6]. We did not concern ourselves with the specific potential, or even the scattering length, for the same reason as stated above. The only issue was finding the value of the Luttinger parameter of our systems. The initial positions of atoms in the simulations were points in 1D crystal lattice. It would make sense, and is often the practice, to generate positions randomly, but this introduces complications since sampling positions from a uniform distribution can lead to atoms starting with extremely high energies due to being very close, so the distribution has to be modified. For the sake of simplicity, we have chosen to start from a lattice, since it does not appear it should affect the results after an initial equilibration phase, and since some of the systems studied here behave as liquids with a degree of structure, it is not even clear the random approach would be superior.

Certain simulation parameters had to be specified before running the simulations. Most notably, the time-step analysis was performed to find a suitable value of time step τ. This entailed a convergence study of total energy, and step $\tau = 0.04\,\text{K}^{-1}$ was chosen since the fitted value of energy at this step was within one standard error from the estimated $\tau \to 0$ limit. This study was only performed at one (largest) density, and the results may vary. However, we expect this value to only become more conservative at other simulated densities for which interactions play less of a role[2]. There are other potential problems that were not addressed in this study of time-step dependence, namely, the convergence of different quantities may also vary and the polymers were not allowed to cross-link to reduce the run time of simulations.

The first set of results comes from PIMC simulations carried out as described. We have

[1] The diluteness of the systems presented here may be brought into question though, especially the densest one with $\rho_0^{-1} \approx 2\sigma$.

[2] See the following sections for a sense of how system evolution is simulated.

attempted to determine the Luttinger parameter by fitting the laws (2.96) and (2.97) to the resulting data on pair correlation functions and OBDMs. The goal was to classify systems of different densities and define our predictions for their behaviour in presence of disorder. Since PIMC can only simulate finite temperatures, several of lowest-temperature data sets were chosen, so that the zero-temperature limit may be assessed. The results were not always reliable, and in some cases we have used the data obtained from zero-temperature diffusion Monte Carlo (DMC) simulations to compare and supplement results. The results on the square of absolute value of winding number were used to determine the superfluid fractions, and we have tested if our systems were in the LL regime by fitting the Galilean-invariant scaling relation (2.101) to PIMC data.

The second set of results were obtained from simulations of systems with disorder, i.e. a randomly perturbed external potential. The perturbation was achieved by introducing a single immovable (infinitely massive) impurity particle at a random position, and specifying its interaction with regular atoms. Each simulation was repeated several times, with the disorder particle at a different position. The interaction potential was chosen to be of a Gaussian shape[3], centred on the position of the impurity

$$V_{\text{imp}} = \varepsilon \exp\left(-\frac{r^2}{2\sigma^2}\right), \tag{3.2}$$

with $\sigma = 0.25\,\text{Å}$. Different normalization constants were used to modify the strength of the interaction. The reason LJ potential was not used is that in pure 1D, any infinite repulsive potential will render winding impossible, thus completely destroying superflow. By fitting the expression (2.100) to superfluid fraction data we have tested robustness of superfluidity in LL systems of different Luttinger parameters.

3.2 Path integral Monte Carlo

3.2.1 Metropolis algorithm and path integral Monte Carlo

Path integral Monte Carlo method is a subclass of Monte Carlo methods that exploits the path integral formalism and quantum-classical isomorphism discussed in the previous chapter. The Monte Carlo class of numerical methods is characterised by the usage of random sampling to obtain results. PIMC calculations usually employ generalizations of the Metropolis algorithm [3], introduced by Metropolis et al. [27]. The Metropolis algorithm is a method that uses Markov-Chain-based sampling. This means that the sampling is achieved by means of an iterative procedure such that the next distribution of a sample (state) depends only on the current

[3]The exception were a set of test simulations that used LJ potential.

state and a probabilistic rule that governs transitions between states. Under certain conditions, the distribution will asymptotically approach the desired distribution. The Metropolis algorithm is suitable for computation of averages of the form [26]

$$\langle f \rangle = \frac{\int f(\boldsymbol{R}) p(\boldsymbol{R}) \, \mathrm{d}\boldsymbol{R}}{\int p(\boldsymbol{R}) \, \mathrm{d}\boldsymbol{R}}. \tag{3.3}$$

Expression (2.6) is essentially of the same form with $\boldsymbol{R} \to \{\boldsymbol{R}, \boldsymbol{R}'\}$, and $p(\boldsymbol{R}) \to \rho(\boldsymbol{R}, \boldsymbol{R}')$. The convolution of this path (see subsection 2.2.2) adds further coordinates, but the substance is unchanged, and therefore this method may be used with path integrals.

Let s and s' be two possible states of a system, and suppose the system currently occupies state s. The transition probability between the states is $P(s \to s') = T(s \to s')A(s \to s')$, where $T(s \to s')$ is an a priori sampling distribution, i.e. the probability of proposing a transition from s to s', and $A(s \to s')$ is the probability of acceptance. The original, and most simple choice of a sampling distribution is a uniform distribution inside a range varied so that the most efficient rate of acceptance is maintained. PIMC usually requires use of different sampling probabilities. If the transition probability is ergodic, there is a unique equilibrium state that will be sampled in the long run. It is the solution of [3]

$$\sum_s p(s) P(s \to s') = p(s'). \tag{3.4}$$

In practice, the desired probability distribution $p(s)$ is known, and the transition probability is chosen to solve the equation (3.4). This is usually achieved by choosing the transition probability that satisfies detailed balance, which is a sufficient condition for (3.4)

$$p(s) P(s \to s') = p(s') P(s' \to s). \tag{3.5}$$

Detailed balance can be satisfied by a simple rule

$$A(s \to s') = \min \left[1, \frac{T(s' \to s) p(s')}{T(s \to s') p(s)} \right] \tag{3.6}$$

In each step of the algorithm, a possible type of transition is picked from the menu, sampled from the sampling probability, and then accepted or rejected according to (3.6).

Once the desired distribution is reached, (3.3) can be calculated numerically by averaging over random walkers. Direct calculation of energy in this way is a trivial example of an *estimator*. Estimators are functions that are used to calculate observables, and different estimators of the same observable can have different statistical error, efficiency, bias, time-step error, and finite-size error [3]. Most notably, the PIMC implementation used in this study uses the virial estimator of energy, and the winding-number estimator of superfluid fraction. We omit any

further discussion of estimators, and refer the reader to reference [3].

3.2.2 The problem of sampling in PIMC

There are two components to sampling the possible microstates of the system, the path sampling, and the sampling of permutations that close the paths. There are many possible "correct" ways of sampling, in the sense that they eventually converge to the right distribution, but in computational methods, efficiency is as much of an issue as correctness, since time and computational resources are limited. The analogue of the classic sampling method used in many other Monte Carlo simulations would be the method of attempting to move a single bead at a time to a random position inside a box whose length is adjusted to achieve close to $50\,\%$ rate of acceptance. This method may be the best example of the peril of making bad sampling choices. It can be shown from the fact that the largest displacement possible is of the order of the thermal wavelength that the computer time needed for the centre of mass of a polymer to diffuse a fixed distance scales unfavourably with M (M^3) for large M. Hence, trying to reduce the time step τ to increase precision will lead to prohibitively long correlation times [3].

A degree of optimization can be achieved by performing "multi-slice" updates. The proposed new positions of a number l of slices belonging to the same world line are sampled from a product of free-particle density matrix terms (propagators) at the inverse temperature $\tau = \beta/M$. A recursive multilevel bisection algorithm is often used [3], namely the *staging* algorithm [13], wherein the midpoint position is generated first from the free-particle propagator at $\tau l/2$, and then quarter point, etc.

Permutation sampling can be achieved in a direct way by attempting cyclic permutations $\mathcal{P}$ with probability $T^*(\mathcal{P}) \propto \rho(\boldsymbol{R}_m, \mathcal{P}\boldsymbol{R}_{m+l}, \tau l)$, normalized so that the probability of choosing any permutation is one. This is equal to the full transition probability since the acceptance rate is $100\,\%$ [4]. A suitable approximation does away with the potential action, and the remaining free-particle density matrix may be factorized into a product of elements of the transition table. After a permutation is performed, a segment of path must be constructed in accordance with the permutation, and this can be done in the same manner as for path sampling. Since this is not the method we applied, we will not go into further detail of this method. This can be found in references [3, 13].

More recently, another kind of permutation sampling, which we have used and will describe in the next section, has gained use. The reason for its emergence, as explained in [12], lays in the fact that the frequency with which long permutation cycles are sampled decreases exponentially with N [5]. Therefore, it becomes increasingly harder to study large systems. Additionally, it is

[4] This is called the heat bath rule, and it is difficult to apply to continuous path sampling due to the infinite number of possible paths.

[5] Long permutation cycles are necessary for studying some quantum properties, most notably they are needed

difficult to distinguish if the reason for the absence of long permutation cycles lays in physics or in non-ergodicity of the sampling method.

3.2.3 Worm algorithm

The worm algorithm (WA) represents an alternative approach to sampling paths that solves some of the problems of the conventional PIMC algorithm [12]. One of the innovations of WA is the ability to operate in the grand canonical ensemble, as presented in [12], but since we work in the canonical ensemble, we only use updates which preserve the total number of atoms.

The configurational space of the WA is extended to include off-diagonal configurations which contain a single open world line, referred to as the *worm*, along with $N-1$ closed world lines. The beads at the two ends of a worm are called the *head* or *Ira* ($\mathcal{I}$), and the *tail* or *Masha* ($\mathcal{M}$). At a given point during simulation, the configuration can be either diagonal or off-diagonal. The diagonal configurations belong to the *Z-sector* of the configurational space, while the off-diagonal ones belong to the *G-sector*, and there are updates that allow for transition between the sectors. The Z-sector configurations enable the calculation of diagonal properties, associated with the partition function Z, while G-sector is necessary to make any topological changes such as winding of the paths[6], and for calculation of the OBDM. A special type of update which acts on the worm takes care of all permutation sampling ergodically, by reconnecting the head of the worm to another world line.

The version of WA that we have used allows seven types of updates. Each of the updates has a certain probability of being proposed, and if proposed, is accepted or rejected according to the standard Metropolis algorithm. We will now describe the possible updates and show their schematic world-line diagram [7] representations.

Two of the possible updates, the *dispace* and *wiggle*, can be performed in both sectors, but are only performed on closed world lines. These are not limited to the WA class of PIMC methods. The displace update is a simple rigid translation of the entire world line. The translation vector is picked randomly, subject to constraint that its magnitude is less than a predetermined maximum length. This length is modified during the simulation in order to optimize acceptance rate. Since the kinetic action is unaffected by a rigid translation, the acceptance probability depends only on the difference in potential action between the initial and proposed configuration. The wiggle update consists of picking a random atom index i, and reconstructing the positions of its beads between slice j_0, also picked at random, and slice j_0+l. This is shown in Figure 3.1. In this case, the value of l is modified to achieve optimal acceptance ratio. The new positions are sampled from the distribution determined by free-particle action, i.e. the product of gaussians for every

to have a non-zero value of the winding-number estimator of superfluid fraction.

[6] Though winding number averages are calculated in the Z-sector.

[7] The x-axis of a world-line diagram represents space, and the y-axis time.

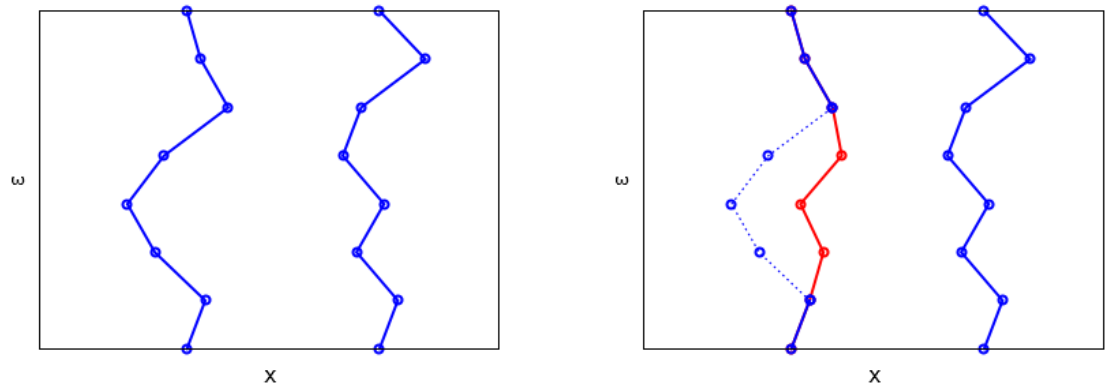

Figure 3.1: *The wiggle update. On the left side, the initial configuration is shown. On the right side, the updated configuration is shown in solid, along with the initial configuration in dashed lines. The images are reproduced with permission from [29].*

link. This is done in multiple steps, according to the staging algorithm. Since kinetic action is exactly the free particle action, this takes care of the kinetic factor in acceptance probability, which, yet again, depends only on the potential action [13, 5] [8]

$$A_{\text{displace/wiggle}} = \min\left[1, \exp\left(\sum_{m=1}^{M} U(\boldsymbol{R}_m, \boldsymbol{R}_{m-1}; \tau) - U(\boldsymbol{R}'_m, \boldsymbol{R}'_{m-1}; \tau)\right)\right], \tag{3.7}$$

where the prime denotes the proposed coordinate, $\tau = \beta/M$, and the summation limits may be replaced by $j_0 + 2$ and $j_0 + l$ in case of the wiggle update.

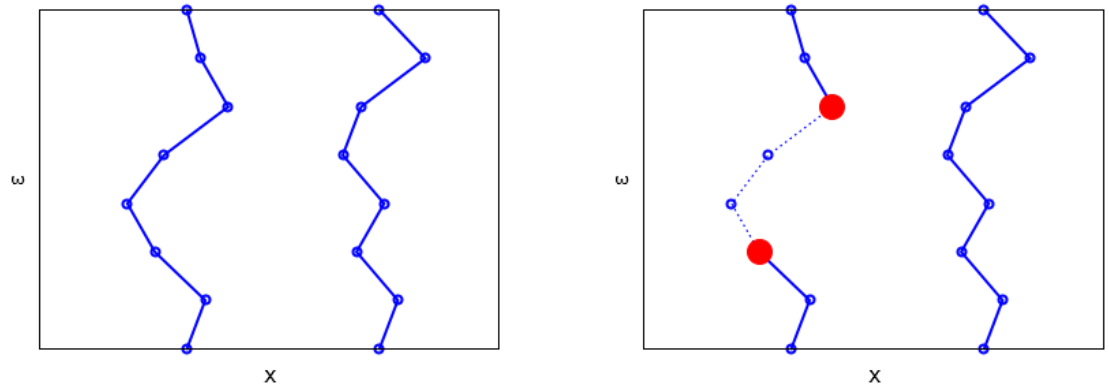

Figure 3.2: *The open update. On the left side, the initial configuration is shown. On the right side, the updated configuration is shown in solid, along with the initial configuration in dashed lines. The images are reproduced with permission from [29].*

Next, two complementary updates switch between the sectors. The *open* update operates only in Z-sector, and it opens one of the closed polymers. This is achieved by randomly selecting a bead $\boldsymbol{r}_{i,j_0}$ and an integer l such that $1 \leq l \leq l_{\max} < M$, and then removing the $l-1$ successive beads $\boldsymbol{r}_{i,m}$ with $m = j_0 + 1, j_0 + 2, \ldots, l_{\max} - 1$. The two end beads now become Ira and

[8] From here on we omit the $1/\hbar$ factor, letting the action absorb it.

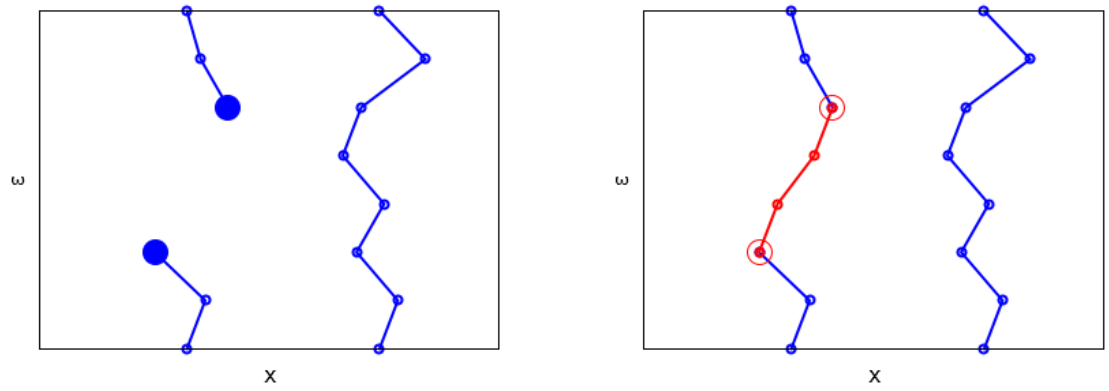

Figure 3.3: *The close update. On the left side, the initial configuration is shown, and on the right side, the updated configuration. The images are reproduced with permission from [29].*

Masha. This is shown in Figure 3.2 The probability of accepting this update is

$$A_{\text{open}} = \min\left[1, C\frac{e^{\Delta U}}{\rho_0(\boldsymbol{r}_{i,j_0+l}, \boldsymbol{r}_{i,j_0}; \tau l)}\right], \tag{3.8}$$

where ΔU is again the difference in the potential action between the initial and proposed configurations, and C is the constant that controls the relative statistics of the two sectors. C and l_{max} are simulation parameters that only affect the efficiency of the simulation [12]. On the other hand, the *close* update, shown in Figure 3.3, operates only in G-sector, and it reconnects Ira and Masha by constructing a path consisting of l beads between them. The number l is the "distance" between the position of Ira and Masha in time. The path is sampled from the free-particle distribution, and the acceptance probability is

$$A_{\text{close}} = \min\left[1, \frac{\rho_0(\boldsymbol{r}_{\mathcal{M}}, \boldsymbol{r}_{\mathcal{I}}; \tau l)\, e^{\Delta U}}{C}\right]. \tag{3.9}$$

The parameters l_{max} and C are the same as before. In this case the move has to be rejected if $l > l_{\text{max}}$.

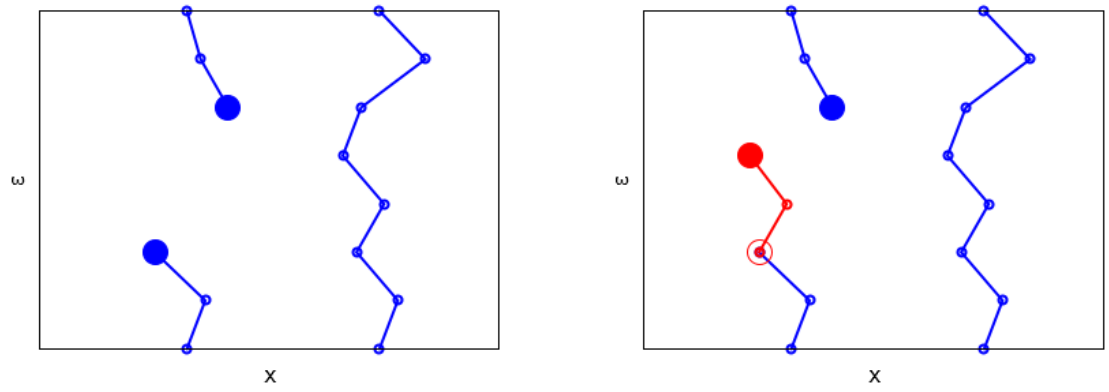

Figure 3.4: *The advance update. On the left side, the initial configuration is shown, and on the right side, the updated configuration. The images are reproduced with permission from [29].*

Another pair of complementary updates operate exclusively in G-sector. The *advance* update (Figure 3.4) moves the head of the worm in space and advances it in time by attaching to it a random number $l < l_{\max}$ of beads sampled from the free-particle distribution. The *recede* update (Figure 3.5 erases $l < l_{\max}$ beads. The update is rejected if l is greater than the number of beads in the worm. The probability of acceptance is

$$A_{\text{advance/recede}} = \min\left[1, e^{\Delta U}\right]. \tag{3.10}$$

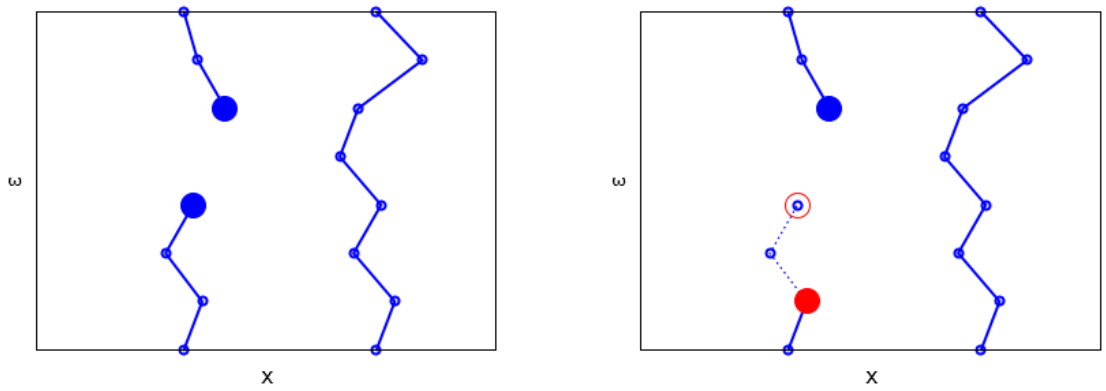

Figure 3.5: *The recede update. On the left side, the initial configuration is shown. On the right side, the updated configuration is shown in solid, along with the initial configuration in dashed lines. The images are reproduced with permission from [29].*

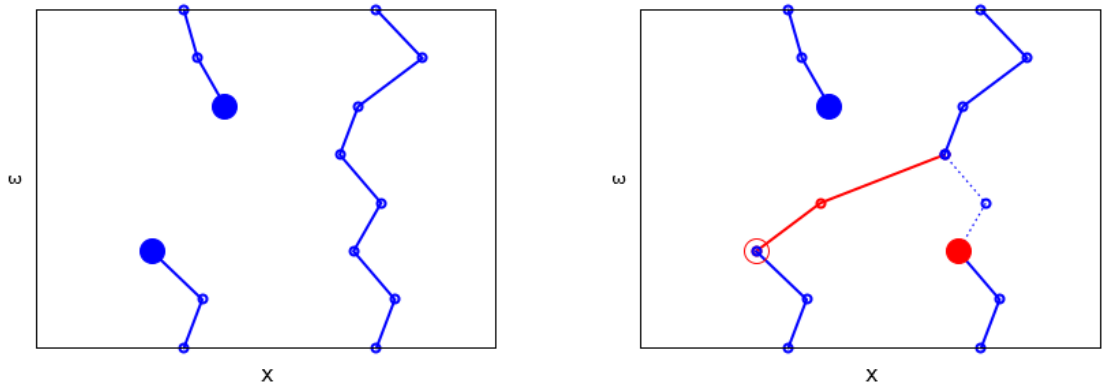

Figure 3.6: *The swap update. On the left side, the initial configuration is shown. On the right side, the updated configuration is shown in solid, along with the initial configuration in dashed lines. The images are reproduced with permission from [29].*

Finally, the *swap* update ensures ergodic and comparatively efficient permutation sampling [12]. Let $j_{\mathcal{I}}$ denote the time slice of the head of the worm, and $l = l_{\max}$. One of the $j_{\mathcal{I}} + l$ beads, denoted by α is chosen with probability proportional to the free particle propagator between $\boldsymbol{r}_{\mathcal{I}}$ and $\boldsymbol{r}_{\alpha}$

$$T_{\alpha} = \frac{\rho_0(\boldsymbol{r}_{\alpha}, \boldsymbol{r}_{\mathcal{I}}; \tau l)}{\Sigma_{\mathcal{I}}}, \tag{3.11}$$

where the normalization is the sum over propagators corresponding to possible choices of α

$$\Sigma_{\mathcal{I}} = \sum_{\sigma} \rho_0(\boldsymbol{r}_\sigma, \boldsymbol{r}_{\mathcal{I}}; \tau l). \tag{3.12}$$

Following the same world line α belongs to back in time from j_α to $j_{\mathcal{I}}$, if any of the beads encountered is Masha, the move is rejected to prevent the worm from closing. If not, let ξ denote the $j_{\mathcal{I}}$-th time slice of the same world line, and let us define $\Sigma_\xi = \sum_\sigma \rho_0(\boldsymbol{r}_\sigma, \boldsymbol{r}_\xi; \tau l)$. An attempt to reconnect world lines is made now. A new path segment is sampled between α and $\mathcal{I}$, the segment between α and ξ is eliminated, and $\mathcal{I}$ and ξ switch labels. This is shown in Figure 3.6. The proposed update is accepted with probability

$$A_{\text{swap}} = \min\left[1, \frac{\Sigma_{\mathcal{I}}}{\Sigma_\xi} e^{\Delta U}\right]. \tag{3.13}$$

Basic strucutre of the program

We thank M. Boninsegni for providing the code for the C++implementation of WA, that made possible obtaining the results that will be presented in this thesis in a reasonable amount of time. The `main` function contains three basic levels of nested loops. We describe what each does in the following paragraphs.

The outermost loops over a predetermined number of blocks. The results we use are block averages of different quantities. The reason for grouping results into blocks is to remove correlation between successive values that is generally present with Markov chain based methods, and tends to decrease the error estimate, which is made under assumption of independent data points. The error estimates tend to rise at first with increasing block size. The size of blocks can be manually optimized by picking one within a range in which the error estimate resembles a plateau. This kind of blocking analysis was performed with estimated errors of energy per particle for a single system, and a block size that was picked was used for all simulations (1000). Note that this analysis was far from comprehensive; preferred block sizes may change for varying system parameters, and perhaps different physical quantities. However we feel that the benefit from additional precision would not justify the time expense, since this is a preliminary study, and is not precision oriented. Different optimal block sizes, were they sought, would likely be of the same order of magnitude.

Each iteration of the middle loop is a "pass" over the system, in the sense that a number of updates greater than or equal to the number of particles is attempted, thus moving the whole system one step. After the step has been made, the diagonal quantities are measured.

The innermost loop is the one that carries out each pass. First a "coin toss" is performed to chose whether to attempt to move a closed or open world line. In the first case, another coin toss decides between calling the `dispace` or `wiggle` methods, and the in second case, one of

the three equally likely possibilities is chosen. The first possibility calls `imove` which attempts either advance or recede update, the second calls `swap`, and the third `close`. Opening a world line will be attempted along with a worm update if the system is in Z-sector. The OBDM is measured in each iteration of the innermost loop. This loop is finished when two conditions are met; the number of iterations must not be less than the number of particles and the worm must be closed in order to measure diagonal properties.

3.2.4 Action approximation

We have already encountered the primitive approximation for the action in section 2.2.2

$$e^{-\tau(\widehat{\mathcal{T}}+\widehat{\mathcal{V}})} = e^{-\tau\widehat{\mathcal{T}}}e^{-\tau\widehat{\mathcal{V}}}, \tag{3.14}$$

and we have noted that it becomes exact in the $\tau \to 0$ limit. Unfortunately, the time step τ can never be made zero in simulations, and the question of its accuracy and efficiency has to be brought up. While simulations with small enough τ will achieve adequate convergence and successful simulation can indeed be achieved with primitive action in some cases, more accurate approximations have been developed. These approximations are appropriate for simulations of large systems, when it is necessary to use larger time steps to increase computational efficiency. We will only briefly present the action that is used in the particular implementation of PIMC that we have used, as laid out in [13]. For details on action approximation methods, see [3].

The potential action of the $(m+1)$-th link takes the form

$$U^{m+1} \equiv U(\boldsymbol{R}_{m+1}, \boldsymbol{R}_m; \tau) = \tau\left[\frac{2}{3}V(\boldsymbol{R}_m) + \tilde{V}(\boldsymbol{R}_m)\right], \tag{3.15}$$

where $V(\boldsymbol{R}_m) \equiv \sum_{i<j} V(|\boldsymbol{r}_{i,m} - \boldsymbol{r}_{j,m}|)$ is the potential energy of the system in configuration $\boldsymbol{R}_m$, assuming it can be expressed as a pairwise sum of terms, and

$$\tilde{V}(\boldsymbol{R}_m) = \begin{cases} \frac{2}{3}V(\boldsymbol{R}_m) + \frac{2\lambda\tau^2}{9}\sum_{i=1}^{N}\left(\boldsymbol{\nabla}_i V(\boldsymbol{R}_m)\right)^2 & , \; m = 2k+1 \\ 0 & , \; m = 2k \end{cases}; \quad k = 0, 1, 2 \ldots ; \tag{3.16}$$

$\boldsymbol{\nabla}_i V(\boldsymbol{R}_m)$ being the gradient of the total potential energy of configuration $\boldsymbol{R}_m$ with respect to the coordinates of the i-th particle $\boldsymbol{r}_{i,m}$. This action approximation is accurate up to terms of order τ^4.

Chapter 4

Results

In this chapter we present a selection of the results obtained from the worm algorithm PIMC and DMC simulations as described in the previous chapter. A section is devoted to determining the value of the Luttinger parameter K of 1D systems of $^4\mathrm{He}$ (see section 3.1) atoms at three different densities, and the following section presents the temperature and length dependence of the fraction of superfluid with and without disorder.

4.1 The Luttinger parameter

In this section we analyse the data on the OBDM and the pair correlation function obtained from PIMC, along with the DMC data on the pair correlation function, the static structure factor[1], and the dependence of the Luttinger parameter on the average density ρ_0. The last is obtained from the compressibility, which is calculated from the equation of state at $0\,\mathrm{K}$ [19]. The main goal is to determine the best fit value of the Luttinger parameter.

4.1.1 The pair correlation function

The pair correlation function is defined as

$$g(r) = (\rho_0)^{-2} \left\langle \widehat{\rho}(r)\widehat{\rho}(0) \right\rangle = (\rho_0 N)^{-1} \sum_{i,j\neq i}^{N} \left\langle \delta(r - |r_i - r_j| \right\rangle . \tag{4.1}$$

[1]The static structure factor is the Fourier transform of the pair density correlation function, but is calculated independently.

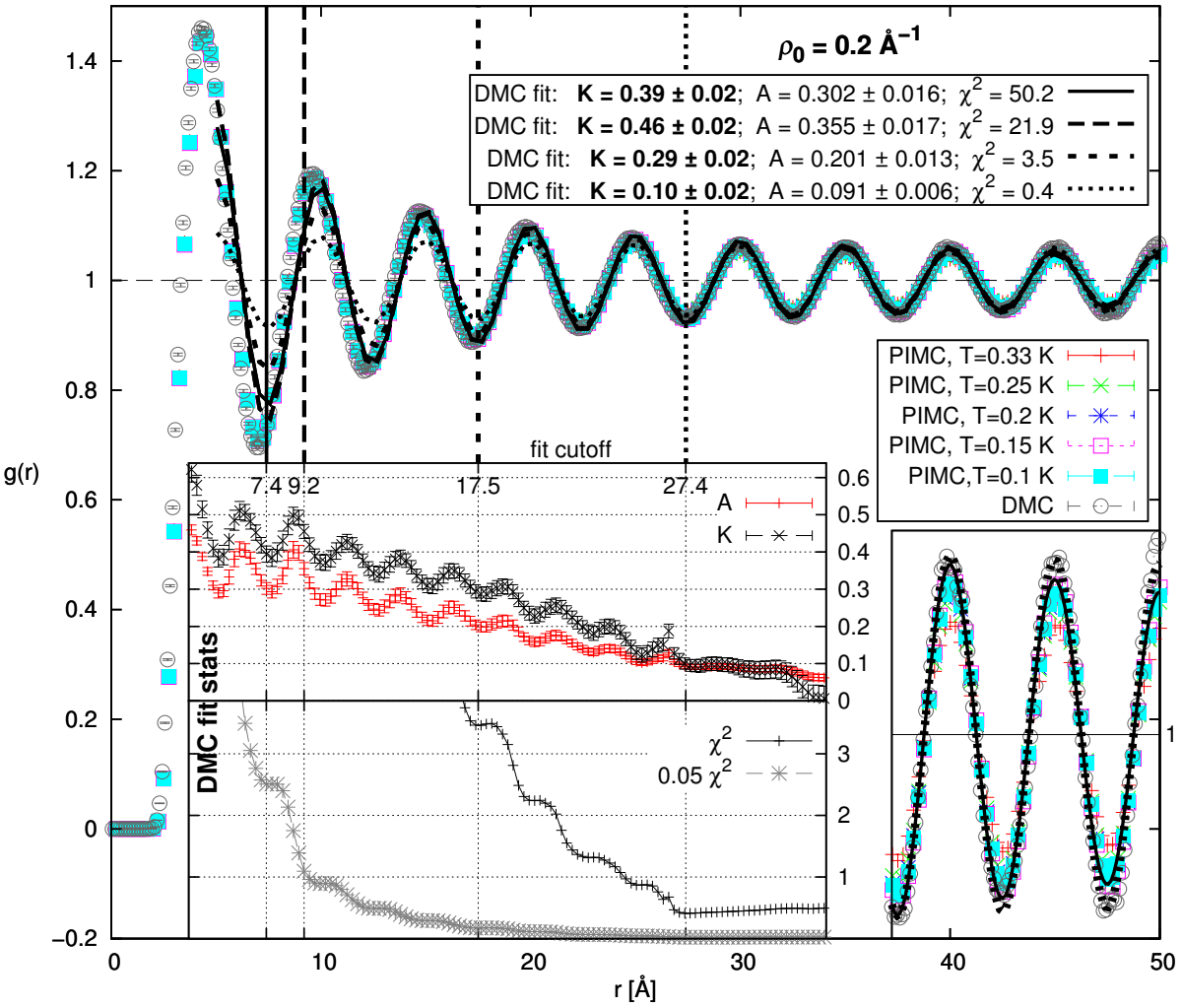

Figure 4.1: *The main graph shows the pair correlation functions calculated from the zero-temperature DMC and PIMC simulations at several temperatures and density* $\rho_0 = 0.2\,\text{Å}^{-1}$*, along with four best-fit functions* (4.2) *differing in the lower fit cutoff. The cutoff positions are marked by vertical lines of the same type as the lines representing the corresponding fitted function. The lower-right inset shows a portion of the main graph with magnified y-axis, and the left inset shows the dependence of the* K*,* A*, and* χ^2 *fit statistics on the cutoff radius. The rescaled* χ^2 *(grey) is included to enable better visualisation. All of the insets share the main x-axis.*

For a LL system in the zero-temperature limit, its asymptotic behaviour is given by the equation (2.96). Keeping only the $m = 1$ term we have

$$g(r) = 1 - \frac{2K}{(2\pi\rho_0 r)^2} + A(\rho_0 r)^{-2K}\cos(2\pi\rho_0 r). \tag{4.2}$$

This expression was fitted to the $g(r)$ data with A and K as adjustable parameters. Since this is an asymptotic expression valid at $r \gg \rho_0^{-1}$, the radii $r \lesssim \rho_0^{-1}$ should be excluded from the fit. The exact cutoff radius chosen can impact the quality of the fit, and it is often unclear which one will produce the most accurate estimate of the parameters. The approach we have adopted is to produce the best fits for a wide range of cutoffs and search for objective indicators of quality

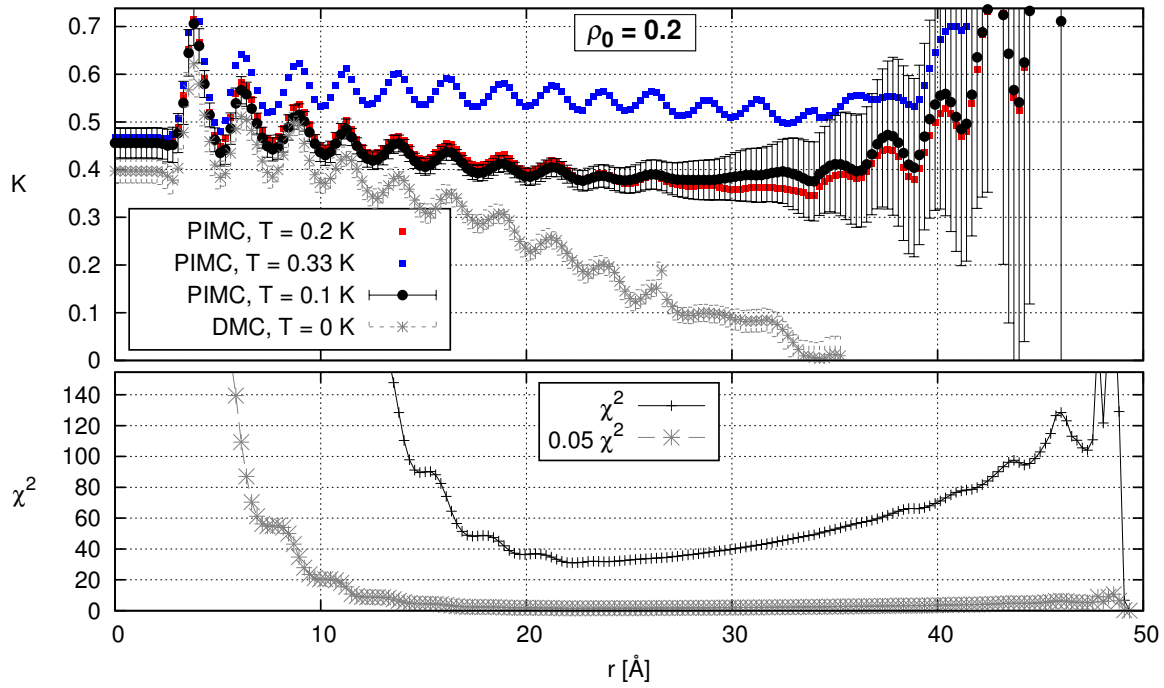

Figure 4.2: *The figure shows the dependence of the PIMC χ^2 and K fit statistics at density $\rho_0 = 0.2\,\text{Å}^{-1}$ and temperature $T = 0.1\,\text{K}$ on lower fit cutoff. The χ^2 is shown in the lower graph alongside with its rescaled values (grey) to enable better visualisation. Additionally, in the upper graph, the K values of several higher temperatures (color) are shown to demonstrate the convergence, and the DMC K values are shown for comparison (grey).*

of the fit, i.e. the reduced[2] chi-square values (χ^2) and the stability of the best-fit parameters, as well as the visual correspondence to the plotted data. When there is a lot of variance between the results, and no obvious way to determine the most correct result, we attempt to asses the reasonable interval for the value of K.

We start with the system at density $\rho_0 = 0.2\,\text{Å}^{-1}$. The PIMC and DMC data are given in Figure 4.1, along with curves fitted to the DMC data for various fit cutoffs. The decaying oscillation of the $g(r)$ characteristic of liquid systems can be seen from the main plot, but the decay appeares to cease at large radii for the DMC data. The PIMC data shows a slight dependence of the amplitude of the peaks on temperature, as can be seen magnified in the bottom-right inset, and the agreement between the zero-temperature DMC and the PIMC data at the lowest temperatures is very good. However, though the decay of oscillation is slow, it does not appear to completely cease for PIMC. This could perhaps be a finite temperature effect, but it is likely that the cessation of the decay is a method-specific numeric effect since the low K values it requires are inconsistent with the rest of the results. The left inset shows the dependence of the DMC fit statistics, namely the χ^2 and the fit parameters, on the cutoff radius. The K parameter drops from around 0.6 to 0, and there appears to be no range of stable values of the fit parameters. The χ^2 values are large for lower cutoffs, and become of order ~ 1 close

[2]Divided by the number of degrees of freedom.

to radius $L/2$. However this region corresponds to unlikely low values of K, close to zero. It is worth noting that the large χ^2 values may be due to underestimate of the uncertainty in the data, but we did not attempt to verify this possibility. The PIMC fit statistics are shown in Figure 4.2. In this case, the values of fit parameters are somewhat more stable, and the global minimum of χ^2 corresponds to $K \sim 0.4$. The PIMC and DMC fits produce similar results up to about $L/8$ radius ($K \sim 0.3$-0.6). We will see from comparison with the structure factor and equation of state results that it is indeed likely that the actual parameter is within a similar range. We also note that the majority of attempted fits, and all of the DMC fits with χ^2 less than two orders of magnitude greater than the minimum (excluding regions of high instability on the right side of Figure 4.2) give the value of K less than 0.5.

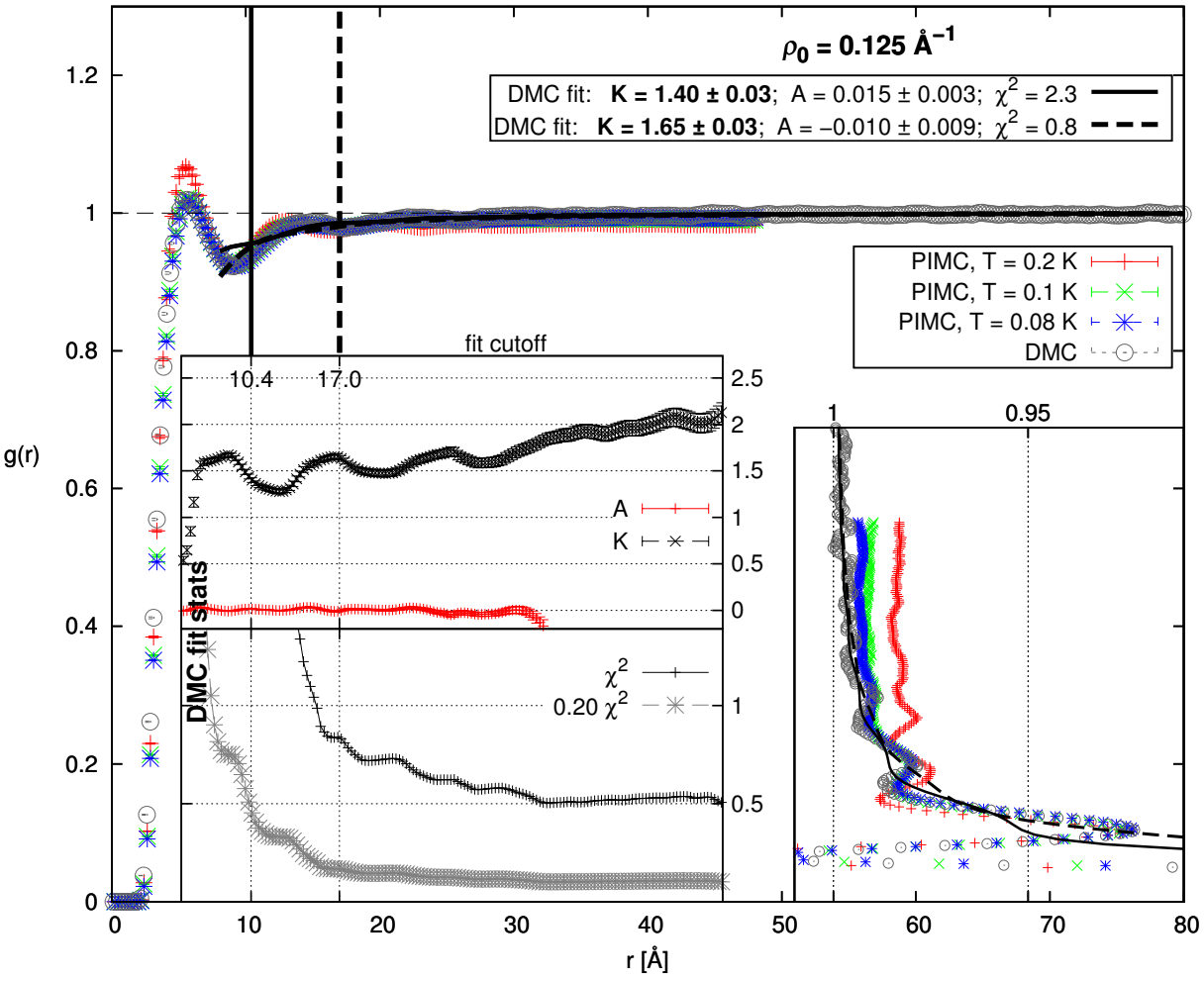

Figure 4.3: *The main graph shows the pair correlation functions calculated from the zero-temperature DMC and PIMC simulations at several temperatures and density $\rho_0 = 0.125\,\text{Å}^{-1}$, along with two best-fit functions* (4.2) *differing in the lower fit cutoff. The cutoff positions are marked by vertical lines of the same type as the lines representing the corresponding fitted function. The lower-right inset shows a portion of the main graph with magnified y-axis (rotated by 90° anticlockwise), and the left inset shows the dependence of the K, A, and χ^2 fit statistics on the cutoff radius. The rescaled χ^2 (grey) is included to enable better visualisation. The left inset shares the main x-axis.*

In Figure 4.3 we show the DMC and PIMC data on pair correlation functions at density

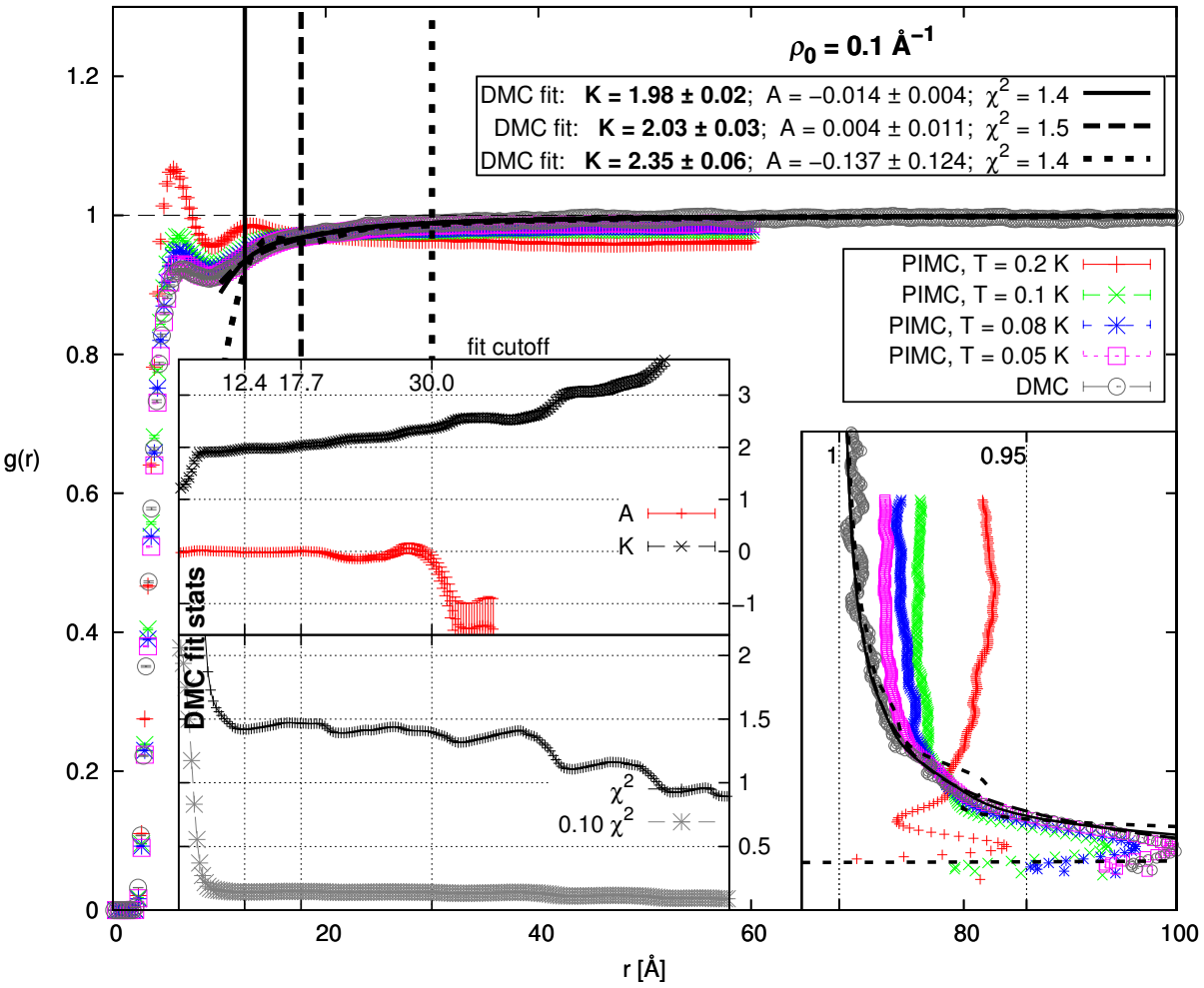

Figure 4.4: *The main graph shows the pair correlation functions calculated from the zero-temperature DMC and PIMC simulations at several temperatures and density* $\rho_0 = 0.1\,\text{Å}^{-1}$*, along with three best-fit functions* (4.2) *differing in the lower fit cutoff. The cutoff positions are marked by vertical lines of the same type as the lines representing the corresponding fitted function. The lower-right inset shows a portion of the main graph with magnified y-axis (rotated by* $90°$ *anticlockwise), and the left inset shows the dependence of the* K*,* A*, and* χ^2 *fit statistics on the cutoff radius. The rescaled* χ^2 *(grey) is included to enable better visualisation. The left inset shares the main x-axis.*

$\rho_0 = 0.125\,\text{Å}^{-1}$, and two fits to DMC data. The oscillations decay very rapidly after the first peak, after which the DMC pair correlation function approaches the constant value of 1 from below. The PIMC pair correlation function appears to approach a lower value, and this value rises toward 1 at lower temperatures. Presumably, the PIMC plot would look very similar to the DMC plot at a low enough temperature, but this was not simulated due to high computational cost of low-temperature PIMC simulations. This can be seen in more detail in the bottom-right inset. As can be seen from the DMC fit statistics inset, the value of the K estimate is fairly stable at $K \sim 1.5 \pm 0.2$ [3] in a region from $\rho_0^{-1} = 8\,\text{Å}$ to about $30\,\text{Å}$, after which it rises above 2 which is implausible both due to its inconsistency with results for smaller cutoffs, reduced stability of

[3] The interval is assessed from the behaviour of the K plot, and is different from the computed errors which tend to be an order of magnitude smaller as can be seen from the legend.

both parameter estimates, and disagreement with estimates obtained from other methods. The χ^2 values are close to one at around $15\,\text{Å}$ and up to $20\,\text{Å}$, indicating good fit quality. We omit the discussion of fits to the PIMC data since they are necessarily of lesser quality due to the discussed finite-temperature effects.

Nearly everything stated in the previous paragraph applies as well to the $\rho_0 = 0.1\,\text{Å}^{-1}$ case, and the graphs are shown in Figure 4.4. In this case, the K estimate can be given at around or slightly above 2, but less than 2.5. The χ^2 values are approximately 1.5, which is less than ideal for a large number of degrees of freedom [4], but probably low enough to allow a decent fit quality.

4.1.2 The structure factor

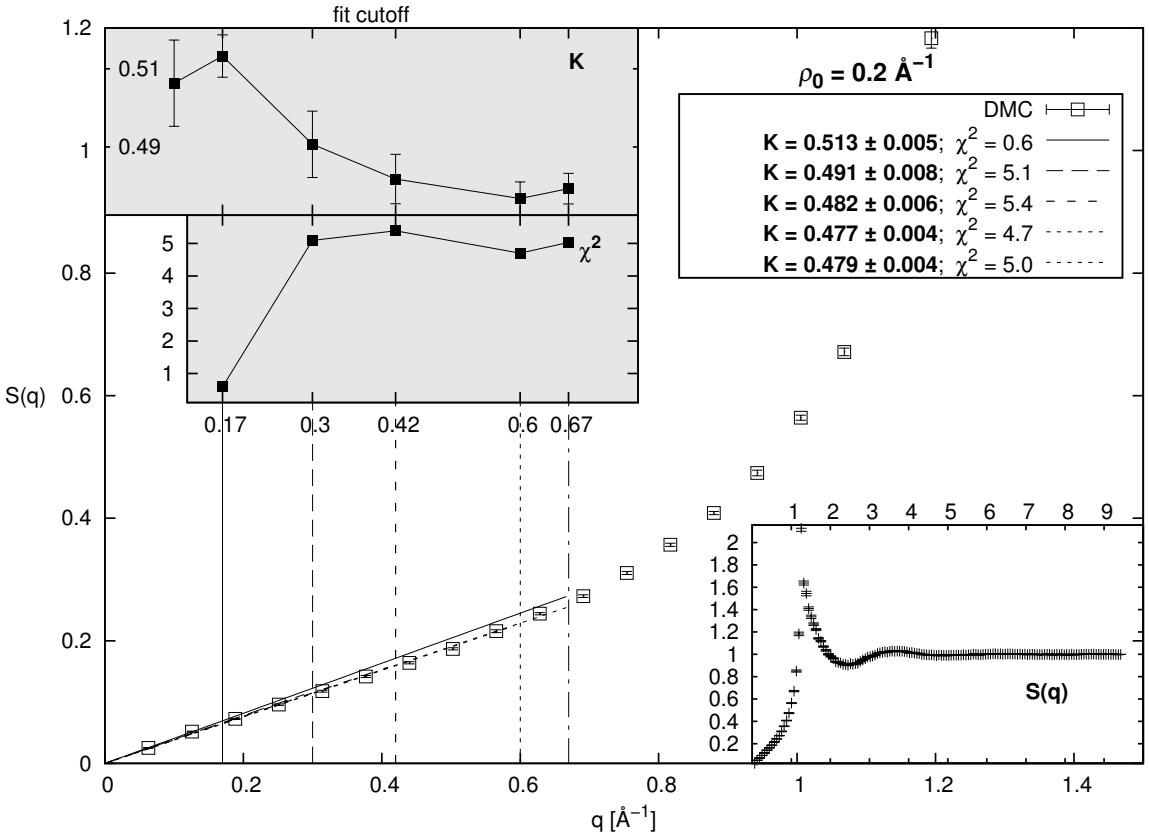

Figure 4.5: *The main graph shows the results of the DMC calculation of the static structure factor at low q and density $\rho_0 = 0.2\,\text{Å}^{-1}$, along with several lines representing the best fit of* (4.4) *to the low q data up to various values of upper fit cutoffs q_c. The q_c positions are marked by vertical lines of the same type as the lines representing the corresponding fitted function. The bottom-right inset shows the full range of q, and the insets on the top left graphically show the dependence of fit statistics on the selected q_c. The leftmost K estimate comes from the linear interpolation between $q = 0$, and the first q point.*

[4] The table of critical values of nonreduced χ^2 can be found at http://www.itl.nist.gov/div898/handbook/eda/section3/eda3674.htm

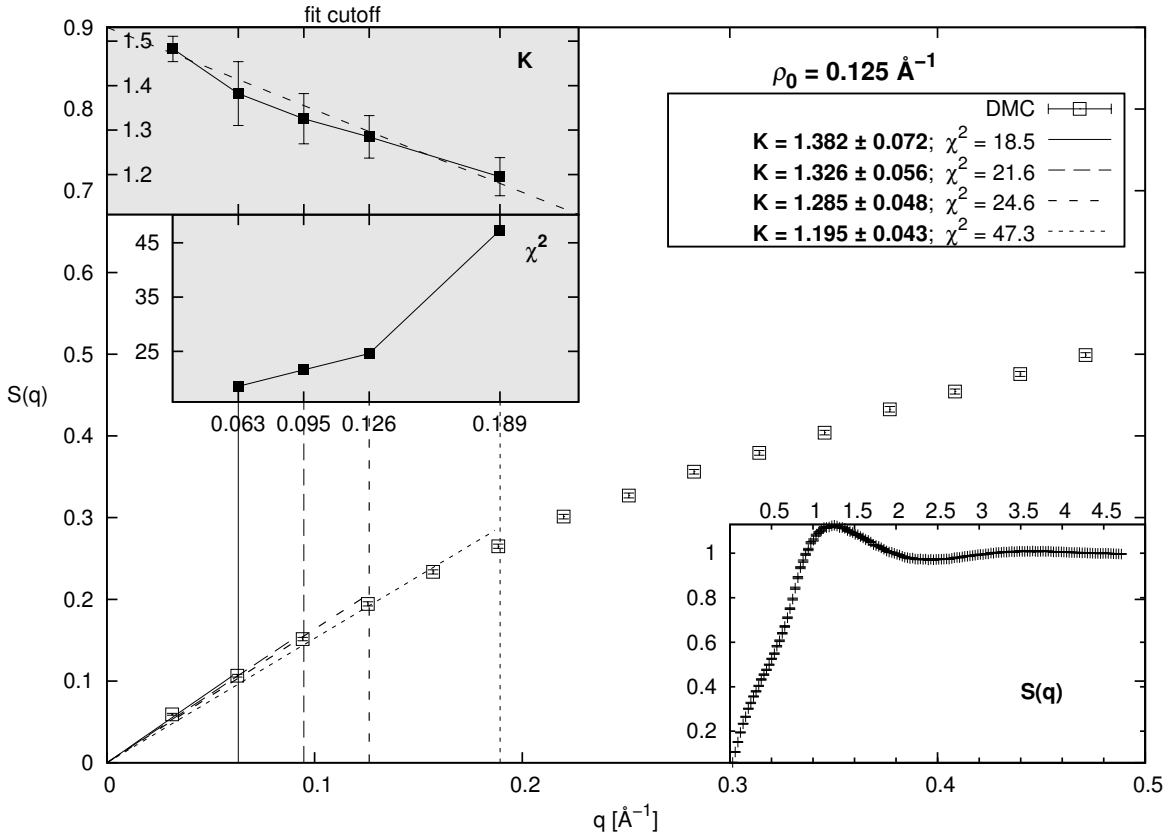

Figure 4.6: *The main graph shows the results of the DMC calculation of the static structure factor at low q and density $\rho_0 = 0.125\,\text{Å}^{-1}$, along with several lines representing the best fit of* (4.4) *to the low q data up to various values of q_c. The q_c positions are marked by vertical lines of the same type as the lines representing the corresponding fitted function. The bottom-right inset shows the full range of q, and the insets on the top left graphically show the dependence of fit statistics on the selected q_c. The leftmost K estimate comes from the linear interpolation between $q = 0$, and the first q point. A simple linear fit to the K estimates is drawn in order to extrapolate the K estimate to the $q \to 0$ limit. The extrapolated value is $K \to 1.53 \pm 0.02$.*

The static structure factor

$$S(q) = \frac{1}{N}\left\langle \sum_{i,j\neq i}^{N} e^{-iq(r_i - r_j)} \right\rangle \tag{4.3}$$

is the reciprocal space analogue of the pair correlation function, which implies that, like the $r \to \infty$ limit of $g(r)$, its behaviour in the $q \to 0$ limit is controlled by K. We expect that[17]

$$K = 2\pi\rho_0 \lim_{q\to 0} \frac{S(q)}{q}, \tag{4.4}$$

and therefore, a function

$$S(q) = \frac{K}{2\pi\rho_0} q \tag{4.5}$$

can be fitted to the data via the parameter K for $q \ll 2\pi\rho_0$. The data on the structure factor were obtained from DMC simulations. The main problem with this method is that q is discrete

for finite box sizes, and the system sometimes has to be very large in order to have enough low q points to obtain a good fit.

The structure factor at density $\rho_0 = 0.2\,\text{Å}^{-1}$ is shown in Figure 4.5, partially in the main graph, and full range is given in one of the insets. The fits were done for various cutoff values q_c up to about $\pi\rho_0$. Except for the $q_c = 0.17\,\text{Å}^{-1}$ fit, the fit quality indicated by χ^2 values is relatively poor (but not terrible), even for the $q_c = 0.3\,\text{Å}^{-1}$ fit which only has three degrees of freedom[5]. However, the one fit of good quality and the manually added value of K obtained from a single q point are both close to 0.51. We may quote the added value and its error as the final estimate $K = 0.51 \pm 0.01$, but note that the uncertainty may be an underestimate.

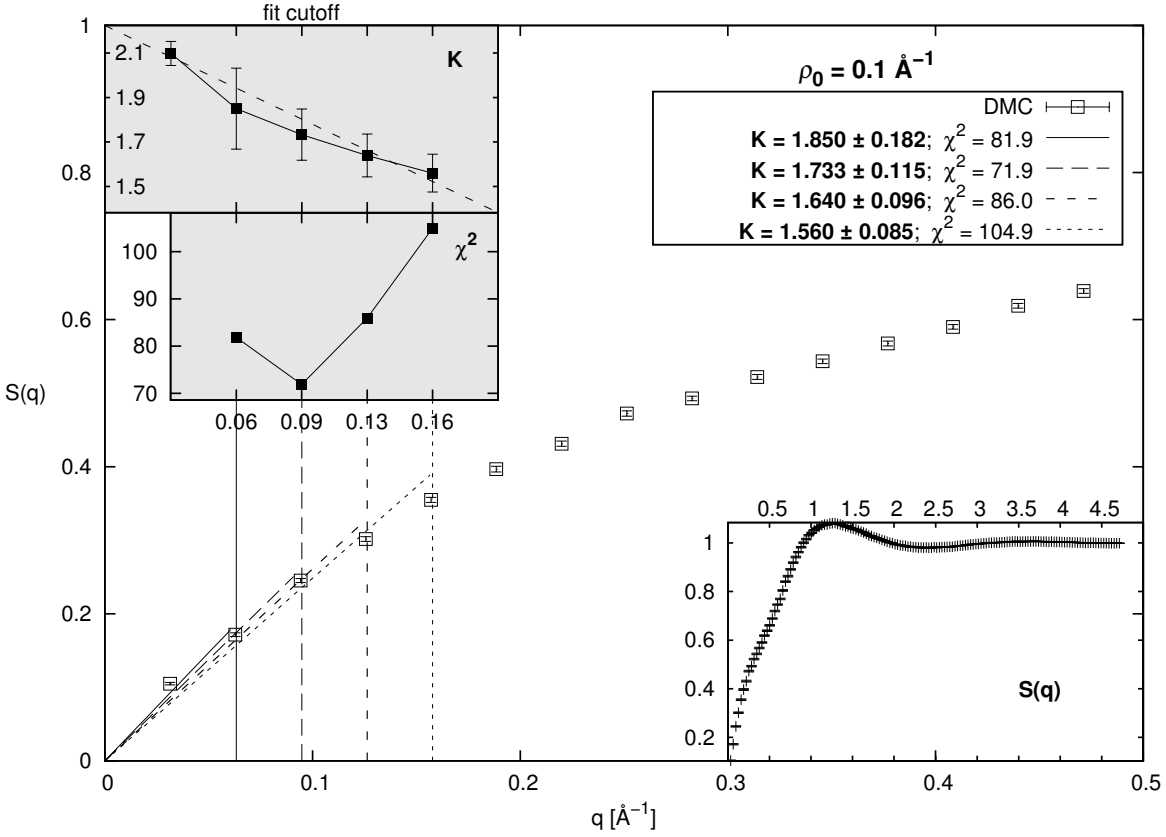

Figure 4.7: *The main graph shows the results of the DMC calculation of the static structure factor at low q and density $\rho_0 = 0.1\,\text{Å}^{-1}$, along with several lines representing the best fit of* (4.4) *to the low q data up to various values of q_c. The q_c positions are marked by vertical lines of the same type as the lines representing the corresponding fitted function. The bottom-right inset shows the full range of q, and the insets on the top left graphically show the dependence of fit statistics on the selected q_c. The leftmost K estimate comes from the linear interpolation between $q = 0$, and the first q point. A simple linear fit to the K estimates is drawn in order to extrapolate the K estimate to the $q \to 0$ limit. The extrapolated value is $K \to 2.22 \pm 0.04$*

The $\rho_0 = 0.125\,\text{Å}^{-1}$ data are shown in Figure 4.6. The range in which a linear fit makes sense is much more restricted than in the previous case. In fact, all of the fits appear to be of poor quality from the χ^2 values, and no K convergence is visible. We have attempted a linear

[5]This sets the $p = 0.99$ critical value below 4.

extrapolation of K to the $q \to 0$ limit. The estimate obtained in this way is $K = 1.53 \pm 0.02$, and is not far off from the single-point K estimate. The correct result is not likely to exceed this estimate significantly, but it may be slightly lower, between 1.3 and 1.5 judging by the two-point fit.

Finally, the $\rho_0 = 0.1\,\text{Å}^{-1}$ data are shown in Figure 4.7. The graph is very similar to the previous case, and there is no need for detailed discussion. The extrapolated value of the Luttinger parameter is $K = 2.22 \pm 0.04$, but the smaller values of K are still plausible, down to about $K = 1.7$.

4.1.3 The one body density matrix

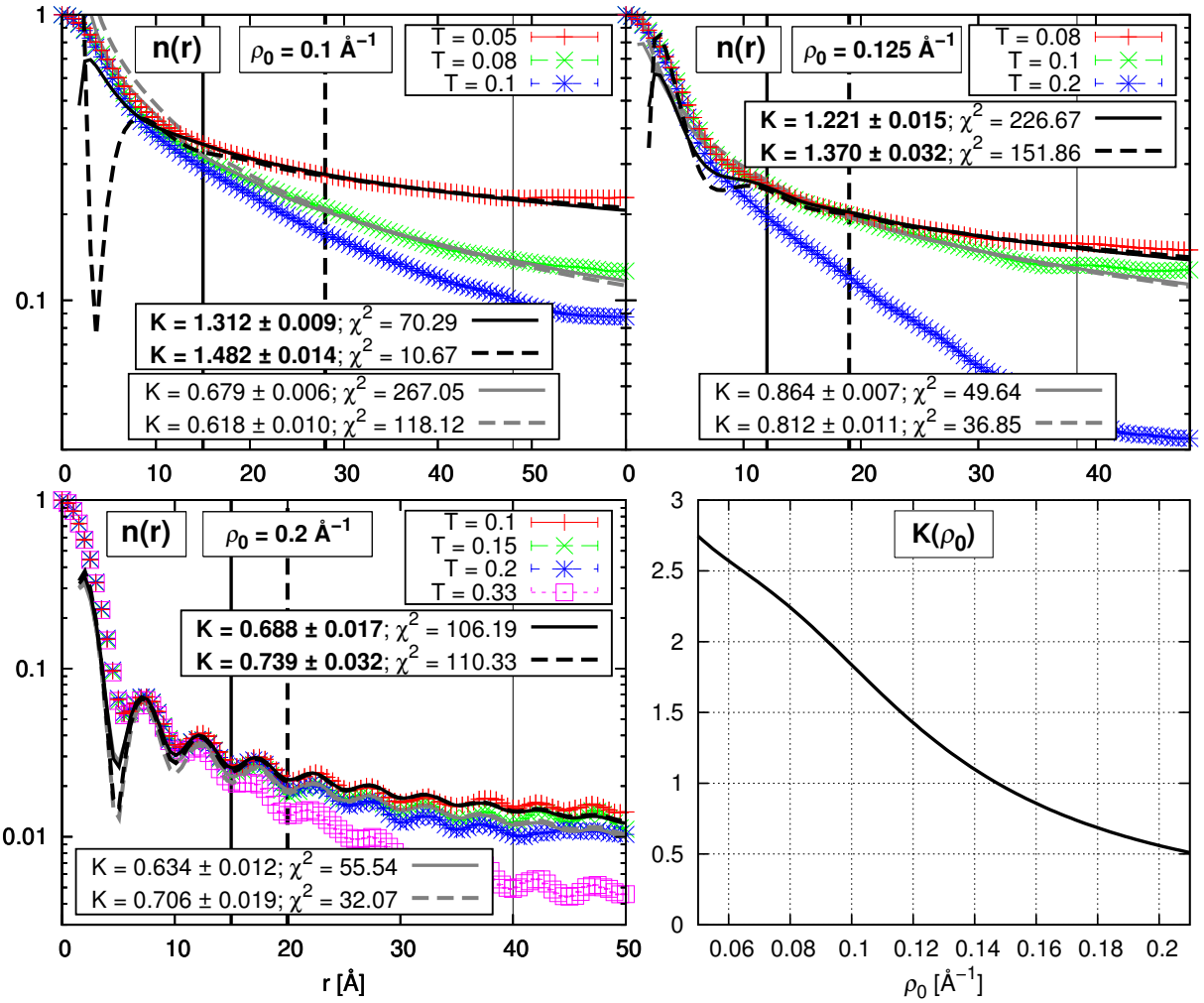

Figure 4.8: *The figure shows the results of the PIMC calculation of the one body density matrix at three average densities and the dependence of the Luttinger parameter K on the average density (bottom-right). The latter is calculated from the zero-temperature average energies (equation of state) obtained from DMC simulations. For each density, the function* (4.6) *fitted to the lowest temperature (black) and the second-lowest temperature (grey) data for two lower cutoff radii is shown. The upper cutoff radius of* $0.1L$ *is used as well, since the results seem to become less reliable, probably due to inefficient sampling. It is marked by a thin vertical line in each of the subplots. The subplots at the top share the same y-axis.*

The one body density matrix was defined in (2.7), and here we present the PIMC results on the OBDM normalized by particle density $n(|r' - r''|)$, so that its value at $n(r = 0)$ is 1. The long-range behaviour in the Luttinger model is given by (2.97), or keeping only first two terms

$$n(r) = (\rho_0 x)^{-\frac{1}{2K}} \left[B_0 + B_1(\rho_0 r)^{-2K} \cos(2\pi\rho_0 r)\right]. \tag{4.6}$$

Fitting (4.6) to the data mostly produced fits of poor quality. We show the fits for the lowest and the second lowest available temperature in Figure 4.8. There is no evidence of convergence toward zero-temperature values of K, except in the case of $\rho_0 = 0.2\,\text{Å}^{-1}$ shown in the bottom-left corner. This is not surprising as we have already seen from the $g(r)$ results that the simulated temperatures are not low enough. The value obtained in the $\rho_0 = 0.2\,\text{Å}^{-1}$ case is between 0.65 and 0.75 which is slightly above previous estimates, and in the case of $\rho_0 = 0.125\,\text{Å}^{-1}$, the estimated interval is between 1.2 and 1.4, slightly below previous estimates. While these results are not too far off from the previous estimates, the result for the density $\rho_0 = 0.1\,\text{Å}^{-1}$ is significantly lower than before at $K \lesssim 1.5$. Clearly, significantly lower temperature is required to successfully approximate the pair correlation function and the OBDM at such a low density. However, since the K estimates tend to rise as the temperature decreases, this can be taken as evidence that $K > 1$ at $\rho_0 = 0.1\,\text{Å}^{-1}$ and $\rho_0 = 0.125\,\text{Å}^{-1}$.

4.1.4 Summary

Here we summarise the results on the Luttinger parameter, and state what may be concluded about its value.

$\rho_0 = 0.2\,\text{Å}^{-1}$ The fits to the pair correlation function seem to imply the value in the $(0.3, 0.6)$ interval, based on combination of PIMC and DMC data, with the PIMC data showing more stability, and is awarded more weight. The DMC static structure factor data leads to a consistent result $K = 0.51 \pm 0.01$, as well as the DMC equation of state which suggests a value between 0.5 and 0.6, as can be read from Figure 4.8. Only the PIMC OBDM data suggest a value above 0.6, and the fits are of low quality. We conclude that the value of K is likely to be in the interval $(0.4, 0.6)$, and it is almost certainly less than 1, which will be relevant after introducing disorder.

$\rho_0 = 0.125\,\text{Å}^{-1}$ Here the DMC $g(r)$ data suggests that K is likely to be in the $(1.3, 1.7)$ interval, the structure factor data suggests a similar interval $(1.3, 1.6)$, and the equation of state gives a value between 1.2 and 1.3. The OBDM gives an interval of $(1.2, 1.4)$, but with low fit quality and questionable convergence to zero-temperature behaviour. K is almost certainly above 1, but it is impossible to verify with available data whether it is below 1.5. Its value probably lies in the interval $(1.2, 1.6)$.

$\boldsymbol{\rho_0 = 0.1}\,\text{Å}^{-1}$ The interval consistent with the DMC $g(r)$ data is $(2, 2.4)$, and $(1.7, 2.3)$ for the structure factor. The equation of state suggests 1.8. We conclude the value is probably above 1.5, with $(1.7, 2.3)$ being the likely interval.

4.2 The superfluid fraction

We have shown over the course of chapter 2 how superfluidity and path integral formalism fit together. At the end of subsection 2.3.1 we have shown the scaling relations that connect the superfluid fraction of a finite LL to its length and temperature. Here we show the data on the superfluid fractions obtained from PIMC simulations with and without disorder.

4.2.1 Systems without disorder

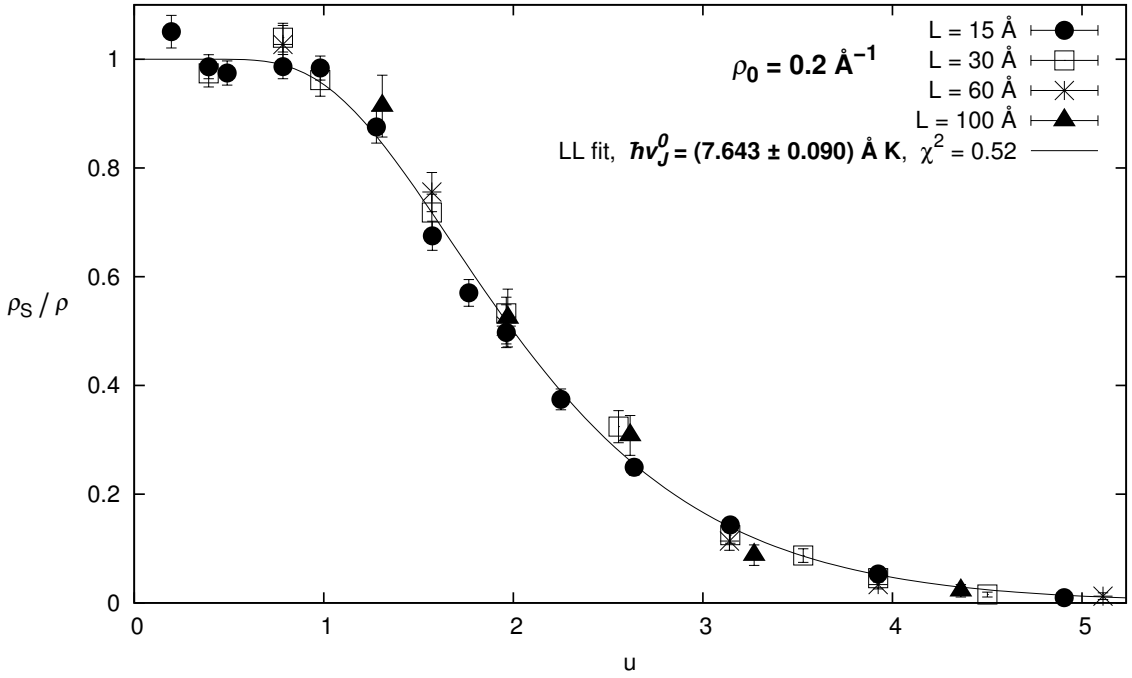

Figure 4.9: *The figure shows the plot of PIMC data on superfluid fractions for a range of temperatures and different box lengths at density $\rho_0 = 0.2\,\text{Å}^{-1}$ without disorder, against the scaling variable $u = \frac{Lk_BT}{\hbar v_J^0}$, along with the scaling function* (4.7) *fitted to the combined data.*

Superfluid fraction estimates obtained using the winding number estimator for systems at density $\rho_0 = 0.2\,\text{Å}^{-1}$ are shown in Figure 4.9. Systems with four different box sizes L were simulated at a range of temperatures. The fitted line is the LL prediction for Galilean invariant systems, with $\hbar v_J^0$ as an adjustable parameter. The first 3 terms in the expansion on the right-

hand side of (2.101) were kept, resulting in the expression

$$\frac{\rho_S}{\rho} = 1 - \frac{8\pi}{u}\frac{e^{-2\pi u} + 4e^{-8\pi u}}{1 + 2e^{-2\pi u} + 2e^{-8\pi u}}, \tag{4.7}$$

where $u = \frac{Lk_BT}{\hbar v_J^0}$. The fit is quite good, which means that there is no significant dependence on either L or T separate from the scaling variable u. The expected value of $\hbar v_J$, $\hbar v_J^0 = 2\pi\lambda\rho_0 = 7,61477$, is within one standard error of the estimated value of the fit parameter, $\hbar v_J^0 = (7.64 \pm 0.09)\,\text{Å K}$.

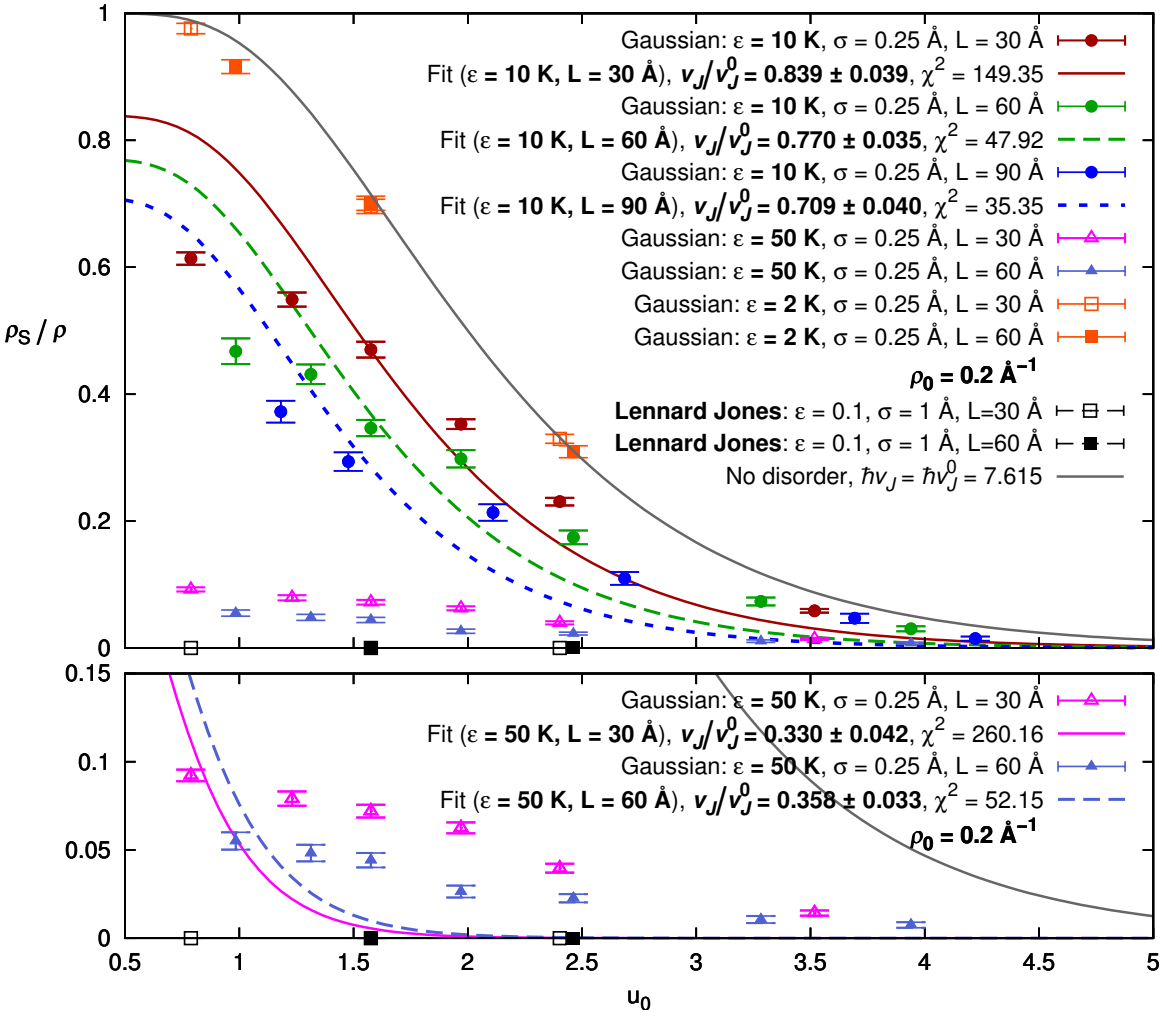

Figure 4.10: *The top panel shows the plot of PIMC data on superfluid fractions against the variable* $u_0 = \frac{Lk_BT}{\hbar v_J^0}$ *for systems of various lengths and temperatures* ($\rho_0 = 0.2\,\text{Å}^{-1}$) *with a single disorder particle. The potential between the disorder particle and regular atoms is either Gaussian-shaped (color) or the Lennard-Jones potential (black), with the potential parameters given in the legend. Fits of the scaling function* (4.8) *to the Gaussian disorder* ($\varepsilon = 10\,\text{K}$) *data are shown in the same color as the points for each box length, and the theoretical prediction for a Galilean invariant system without disorder is shown in grey. The bottom panel shows the fits to the* $\varepsilon = 50\,\text{K}$ *data. Both panels share the same x-axes. The data points are the average of several* (n) *simulations with different randomly selected positions of the impurity. The errors are calculated from* $\sigma = \frac{1}{n}\sqrt{\sum_i^n \sigma_i^2}$.

4.2.2 Systems with disorder

We begin by noting that the additional particle of impurity is expected to have the effect of decreasing effective density by excluding a part of the volume. However, if simply the range of the disorder potential is excluded in calculation of ρ_0, the effect on the results is of little significance.

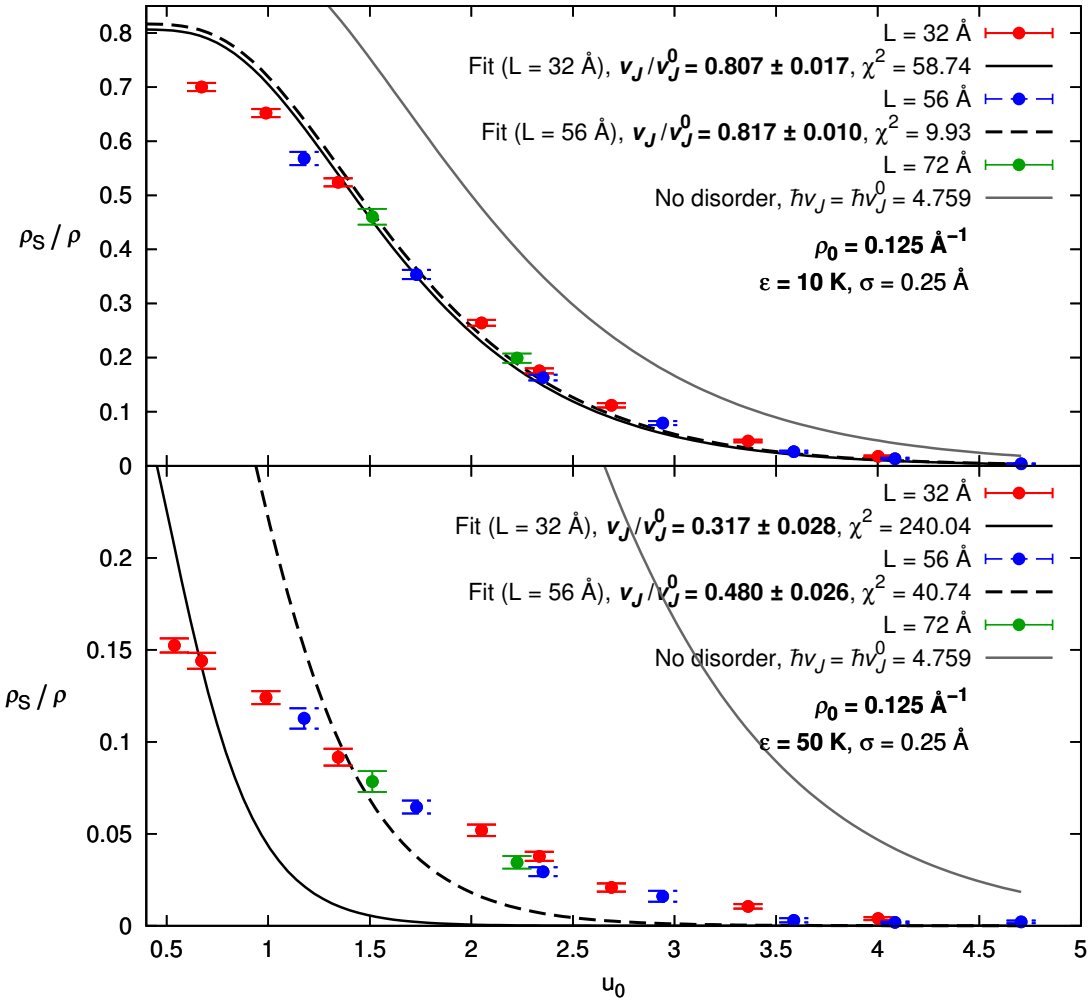

Figure 4.11: *The top panel shows the plot of PIMC data on superfluid fractions against the scaling variable* $u_0 = \frac{Lk_BT}{\hbar v_J^0}$ *for systems of various lengths and temperatures* ($\rho_0 = 0.125\,\text{Å}^{-1}$) *with a single disorder particle. The potential between the disorder particle and regular atoms is Gaussian-shaped with* $\varepsilon = 10\,\text{K}$. *Fits of the scaling function* (4.8) *to the data for two of the box lengths are shown, and the theoretical prediction for a Galilean invariant system without disorder is shown in grey. The bottom panel shows the fits to the* $\varepsilon = 50\,\text{K}$ *data. Both panels share the same x-axes. The data points are the average of several* (n) *simulations with different randomly selected positions of the impurity. The errors are calculated from* $\sigma = \frac{1}{n}\sqrt{\sum_i^n \sigma_i^2}$.

The scaling relation used in previous subsections assumes Galilean invariance, and requires that $\rho_S/\rho \to 1$ as $T \to 0$. Instead, we fit the data on systems with disorder to the expression

(2.100), keeping only the first three terms in expansion:

$$\frac{\rho_S}{\rho} = \frac{2\pi L k_B T}{\hbar v_J^0} \frac{\exp\left(-\frac{\pi}{2} u_0 \frac{v_J^0}{v_J}\right) + 4\exp\left(-\frac{4\pi}{2} u_0 \frac{v_J^0}{v_J}\right)}{1 + 2\exp\left(-\frac{\pi}{2} u_0 \frac{v_J^0}{v_J}\right) + 2\exp\left(-\frac{4\pi}{2} u_0 \frac{v_J^0}{v_J}\right)}, \tag{4.8}$$

v_J^0/v_J being an adjustable parameter, and $u_0\, v_J^0/v_J = u$.

In Figure 4.10 we see the superfluid fraction data for $\rho_0 = 0.2\,\text{Å}^{-1}$ systems with disorder of varying "magnitude"[6] , represented by the normalization parameter ε of the Gaussian potential. Evidently, the magnitude of the disorder affects the resulting fraction, but the fraction does not vanish, except in the case of the unbounded LJ potential. The fractions are very weakly affected in case of $\varepsilon = 2\,\text{K}$, which is an order of magnitude larger than the measured average energies per particle at this density ($\sim 0.4K$). The disorder of $\varepsilon = 10\,\text{K}$ magnitude visibly destroys the u-scaling. The different box lengths are differently affected, with the fraction being more suppressed for larger lengths. The fits to the scaling relation are visibly poor, and χ^2 values are high. The fractions of systems with $\varepsilon = 50\,\text{K}$ are almost completely suppressed.

The top and bottom panels in Figure 4.11 show the $\rho_0 = 0.125\,\text{Å}^{-1}$ data for different disorder magnitudes. The lower-magnitude data on the top appear to be better described by the scaling relation than the $\rho_0 = 0.2\,\text{Å}^{-1}$ data. However, there is visible disagreement between the fits and the data, especially in the low u region, and the χ^2 values are still quite high (although lower for each box length than earlier). The bottom, higher-magnitude data does not show any indication of obeying the predicted scaling relation. However, in both cases there is little difference between different box lengths, as evidenced by the nearly same value of the fit parameter in the lower-magnitude case.

The same discussion applies to the $\rho_0 = 0.1\,\text{Å}^{-1}$ case in Figure 4.12. The deviation from the scaling relation fit is qualitatively the same as in the previous case. However, we see slightly better evidence of breakdown of u-scaling, since the ρ_S/ρ values in the bottom panel appear slightly more suppressed for larger box length.

In summary, addition of disorder suppresses the values of the superfluid fraction and, at least in case of $\rho_0 = 0.2\,\text{Å}^{-1}$ for which $K < 1$, destroys the u-scaling. For the two lower densities ($K > 1$), the scaling appears to be mostly, but perhaps not entirely, preserved. The discussed scaling relation fits the lower-magnitude disorder data better, but there are visible deviations.

[6] We introduce this as an internal shorthand to differentiate between cases differing exclusively in the normalization parameter of the Gaussian.

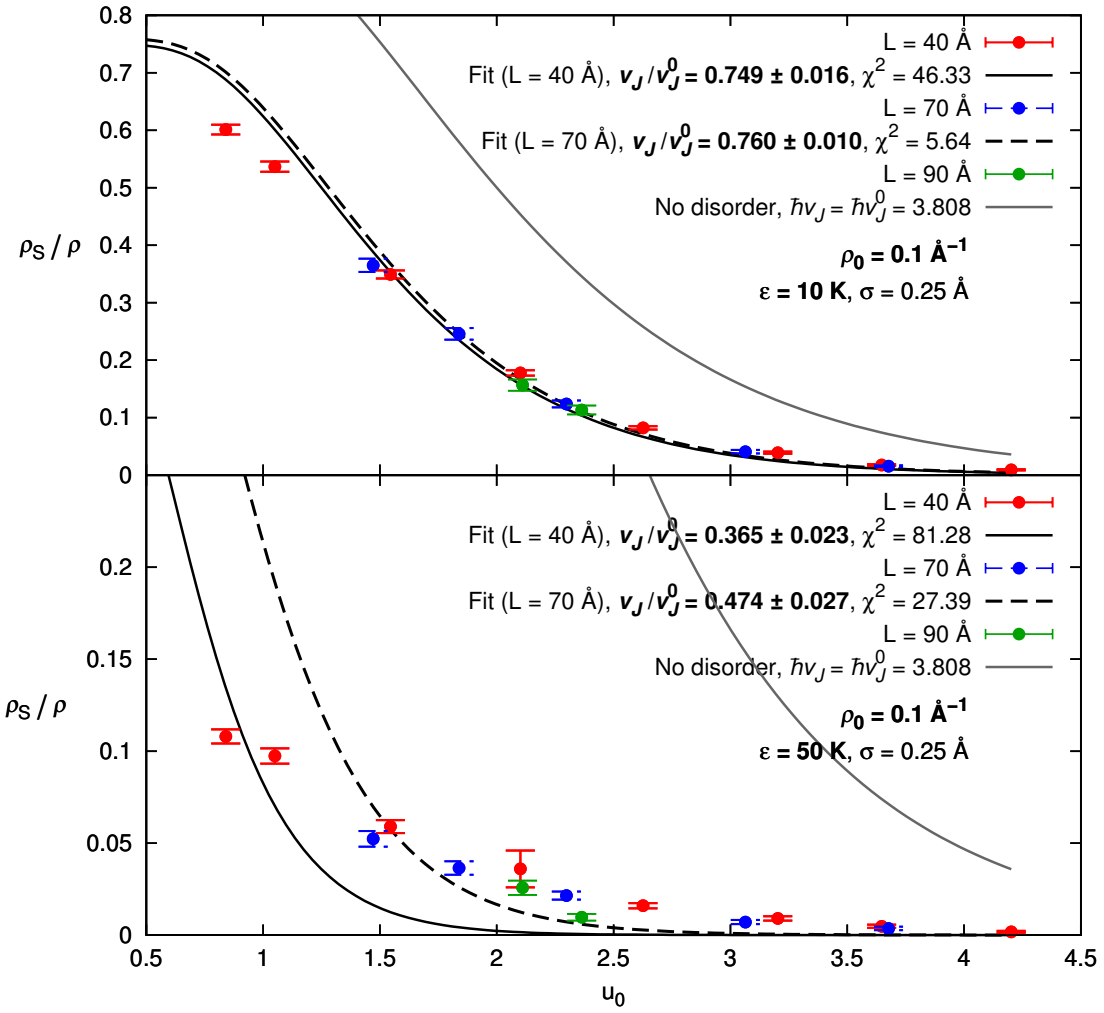

Figure 4.12: *The top panel shows the plot of PIMC data on superfluid fractions against the scaling variable* $u_0 = \frac{Lk_BT}{\hbar v_J^0}$ *for systems of various lengths and temperatures* ($\rho_0 = 0.1\,\text{Å}^{-1}$) *with a single disorder particle. The potential between the disorder particle and regular atoms is Gaussian-shaped with* $\varepsilon = 10\,\text{K}$. *Fits of the scaling function* (4.8) *to the data for two of the box lengths are shown, and the theoretical prediction for a Galilean invariant system without disorder is shown in grey. The bottom panel shows the fits to the* $\varepsilon = 50\,\text{K}$ *data. Both panels share the same x-axes. The data points are the average of several* (n) *simulations with different randomly selected positions of the impurity. The errors are calculated from* $\sigma = \frac{1}{n}\sqrt{\sum_i^n \sigma_i^2}$.

Chapter 5

Discussion

5.1 Agreement with LL model for systems without disorder

We expect the asymptotic behaviour of correlation functions studied here, as well as superfluid fraction scaling, to be consistent with the predictions of the LL model in absence of disorder. Verification of this prediction is not the main focus here, but lack of agreement would invalidate our discussion of systems with disorder. We have seen from the results of section 4.1 that the asymptotic properties of the pair correlation function and OBDM are in qualitative (and visual) agreement with the LL prediction, at least for systems for which we can be reasonably sure finite-temperature effects do not have a major impact and sampling is sufficient. Quantitative results on χ^2 values may raise some doubts in case of PIMC data on $g(r)$ and OBDM at $\rho_0 = 0.2\,\text{Å}^{-1}$, but this is likely to be due to unreliability of results. Deviations from prediction could stem from minor effects of finite temperature and problems with numerical precision, sampling or value estimation. On the other hand, the DMC structure factor allows better fits, and gives consistent results for K. This, along with the qualitative agreement of $g(r)$ and the excellent agreement of superfluid fraction results with the model prediction (Figure 4.9), demonstrates the applicability of the LL theory in this case. The results obtained by others studying similar systems (e.g. [16]) further support this conclusion. For other densities, the DMC results on $g(r)$ and the structure factor show good agreement with the LL model. The fits to $g(r)$ data are good, and the structure factor gives consistent results, despite problems caused by small system sizes. The PIMC results on $g(r)$ seem to approach the DMC ones as temperature drops. Unfortunately, the available OBDM results do not allow unambiguous conclusion.

The behaviour of OBDM warrants separate discussion. We see from Figure 4.8 that it appears to tend to a finite value near the end of the box in some cases. This would imply the existence of off-diagonal long-range order, i.e. Bose-Einstein condensation. This is impossible since we are dealing with a 1D system. Even algebraic order should not be possible at a finite temperature,

and the OBDM can only be approximately described by an algebraically decaying function at short enough distances [20]. We can see from the figure that this appears to happen invariably near the end of the available interval. This has indeed been our experience even when working with the same density systems of different length. We conclude that this effect is most likely not physical, but a problem with finite-size simulations.

5.2 Classification of systems without disorder

The predictions of the LL model for the behaviour of the simulated systems is based on the value of the Luttinger parameter K. The results on K were presented in section 4.1.

In presence of disorder, systems of noninteracting particles can undergo Anderson localization, characterized by exponential decay of single-particle eigenstates [18, 19]. The existence of a localized phase of 1D interacting bosons was shown in [21]. This phase, termed *Bose glass*, is an insulator, i.e. there is no superfluidity due to localization. It is predicted that the transition between superfluid and Bose glass (SF-BG) occurs at $K_c = 3/2$ [21, 22], hence we should observe no superfluidity in systems of $K < 3/2$. However, the full picture is more complicated. Under conditions of dilute disorder and above above a certain finite temperature, a system can remain superfluid down to $K = 1$ [23, 24]. Furthermore, as the disorder strength is increased the transition to the localized phase has also been predicted for $K > 3/2$ [28]. However, different scenarios have been proposed and the issue is still a matter of debate.

As we have seen from figures 4.1 and 4.2, the asymptotic behaviour of $g(r)$ of $\rho_0 = 0.2\,\text{Å}^{-1}$ systems obtained from PIMC simulations is not entirely consistent with those of DMC simulations. We have already concluded that this is more likely to be due to problems with the DMC simulation, rather than finite-temperature effects. Either way, the slow decay of oscillations, and the peak in structure factor at $q \approx 2\pi\rho_0$ indicate solid-like properties. Since most fits to the $g(r)$ give $K < 0.5$, this would place the system in the so-called *quasi-solid* regime [19], but the results are not clear enough to determine this with high certainty. However, it is enough for our purposes to categorize this system as a $K < 1$ system. This allows us to make a prediction that introduction of even localized disorder in form of a single particle should completely suppress superflow.

As we have seen, we can conclude with a high degree of confidence that $K > 1$ at density $\rho_0 = 0.125\,\text{Å}^{-1}$. This means that LL model predicts robustness of superfluid response at least to a localized disordered perturbation, which is the case we have studied. There is some indication that $K < 1.5$, but this is unclear. If true, this would mean that superfluidity should be suppressed by addition of several impurities at random positions. The most straightforward way to determine the value of K more precisely would be to determine the structure factor for larger systems. Alternatively, one could use a system at a slightly higher density. However, we

did not attempt to test this prediction here. On the other hand, it is fairly certain that $K > 1.5$ for systems at $\rho_0 = 0.1\,\text{Å}^{-1}$. These systems should therefore be robust to disorder in a more general sense, as long as it is sufficiently weak.

5.3 Agreement with the LL prediction for disordered systems

The destruction of u-scaling after adding an impurity to a $K < 1$ system clearly shows that the system is no longer in LL regime. On the other hand, the u-scaling appears to remain valid (with possible slight deviations) for the two $K > 1$ systems. This is in accordance with the prediction in the sense that there is a qualitative difference between $K < 1$ and $K > 1$ systems. However, the superfluid fraction does not vanish as expected in the $K < 1$ case, and is in fact very slightly affected for disorder potential of the smallest magnitude shown in Figure 4.10. Since the superfluid fraction decreases with L, we speculate that it eventually converges to zero. This is straightforward to check, but will require lengthy simulations. We note that these results are in accordance with those of reference [17].

The validity of the LL prediction in $K > 1$ case is unclear. While results may be consistent with u-scaling, the scaling relation probably has to differ from the one predicted to explain the observed behaviour. Agreement with the scaling relation (2.100) is much better for smaller disorder magnitude in both $K > 1$ cases, but even here, the deviations do not seem to be due to chance, since in both cases the fitted function overshoots the calculated ρ_S/ρ values at low u by a margin much larger than the error estimate. We can ascertain by observing the fluctuations of ρ_S/ρ in all of the figures of section 4.2 that the true statistical errors are not significantly larger than the typical estimate. The lack of apparent systematic bias in Figure 4.9 lends some credibility to the results, but since the circumstances are different, we would not be entirely justified in dismissing this possibility.

If the scaling relation is changed, this would imply a correction to the LL Hamiltonian (2.84) would be necessary to explain the physical properties of this class of systems in the presence of disorder. However, besides systematic bias, we believe there is another possible explanation for this effect, based on the relative impact of interaction with disorder on particles of different energy, that would have to be excluded before accepting the necessity of any modifications to the LL model.

We have seen from the PIMC pair correlation function and the OBDM that the $K > 1$ systems were not simulated at a low enough temperature to achieve convergence to $T = 0\,\text{K}$ values. A cursory study of energy dependence (see Figure 5.1) on temperature of systems without disorder shows the dependence is significant down to $T = 0.1\,\text{K}$, which is only slightly higher than the lowest temperature used in disorder calculations ($0.09\,\text{K}$). Suppression of superfluid fractions in disordered systems is clearly more pronounced at higher disorder magnitude, and

we assume that this is controlled by its value relative to the average energy. Since the energy decreases together with temperature, and hence with u (L is kept constant), the relative magnitude of disorder increases at low u. If this hypothesis is correct, we should not expect u-scaling, except approximately for small enough Δu. The scaling would remain valid, however, if the magnitude of disorder is varied with temperature so that the relative magnitude remains constant. Therefore, this hypothesis may be tested by fitting (2.100) to the data obtained in this way. Another way to test the hypothesis is to extend the range of simulated temperatures for systems of larger size so that the data includes points at equally low u as that of smaller size. We would expect to see a breakdown of u-scaling with systems of larger size having smaller ρ_S/ρ at low u. This is a slightly more straightforward, but less robust test.

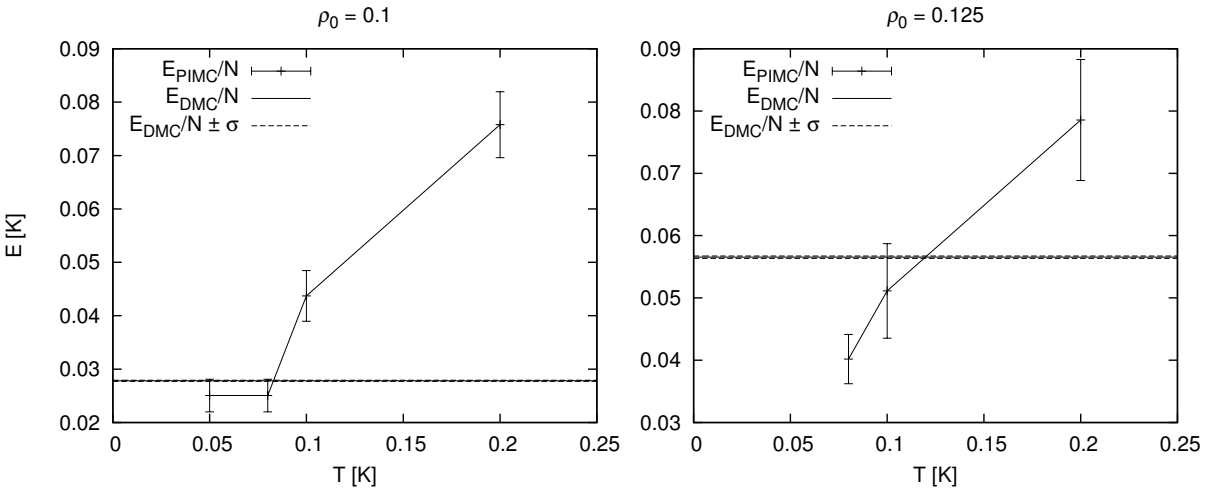

Figure 5.1: *Dependence of the average PIMC energy on temperature. The horizontal lines represent the value of the DMC zero-temperature average energy and its error estimate.*

Chapter 6

Conclusion

We have studied a series of cold one-dimensional Bose systems via the worm algortihm path integral Monte Carlo computational method, and to an extent the diffusion Monte Carlo method. Our aim was to test the applicability of the Tomonaga-Luttinger liquid theory to these systems, especially in presence of disorder.

Our findings on systems without disorder suggest agreement with the Luttinger liquid predictions. Upon introducing dilute disorder, the systems show two different patterns of behaviour. The first pattern, observed in case of the largest simulated density and the Luttinger parameter value $K < 1$, is the complete cessation of u-scaling predicted by the LL model, meaning that the superfluid fractions show separate dependence on temperature and size of the system. The superfluid fractions are not completely suppressed but since they decrease with increasing system size for equal u, we did not discard the possibility that the system sizes were not large enough for localization to achieve full effect. Further research on this is needed. The second pattern was observed in cases of the two $K > 1$ systems, of which at least in one, but possibly in both cases, K was larger than $3/2$. It is characterized by a u-scaling with only minor possible deviations in the simulated range. The u-dependence is not well modelled by the predicted relation, and it is not clear if this implies inapplicability of the LL model. Other possibilities considered are systematic bias and the effect of varying ratio of the average energy to the height of the disorder-related potential barrier.

The results seem to be reconcilable with the predictions of the LL model. However, more research is needed to reach firm conclusions. Tests were proposed in the discussion to verify the convergence of large system sizes to zero superfluid fractions in $K < 1$ systems, and to see if the deviations from the predicted scaling relation in $K > 1$ systems are due to variance in the average energy. Additional convergence tests should also be performed to check the quality of sampling, optimize simulation parameters, and reduce the possibility of biased results. Aside from this, additional densities with more precisely determined K values should be simulated to find the critical value of K. Systems with nondilute disorder should be simulated in order

to see if this results in different a critical value, and if it corresponds to the predicted value of $K_c = 3/2$ for SF-BG transition in case of nondilute disorder.

7 Bibliography

[1] Feynman, R. P. 1972. *Statistical mechanics: a set of lectures.* Reading, Mass: W.A. Benjamin.

[2] Feynman, R. P. 1948. *Space-time approach to non-relativistic quantum mechanics*, Rev. Mod. Phys., **20** (2), 367

[3] Ceperley, D. M. 1995. *Path integrals in the theory of condensed helium*, Rev. Mod. Phys. **67** (2), 279

[4] Coleman, A. J., Yukalov, V. I. 1992. *Order indices for boson density matrices*, Il Nuovo Cimento B, **107**(5), 535

[5] Rota, R 2011., *Path Integral Monte Carlo and Bose-Einstein condensation in quantum fluids and solids* (doctoral thesis), Universitat Politècnica de Catalunya

[6] Pitaevskii, L. P., Stringari, S. 2003. *Bose-Einstein condensation*. Oxford, UK: Oxford University press

[7] Pethick, C. J., Smith, H. 2008. *Bose-Einstein condensation in dilute gases* (2nd ed.). Cambridge, UK: Cambridge University Press

[8] Lifshitz, E. M., Pitaevskii, L. P. 1980. *Course of theoretical physics. Statistical physics, part 2: theory of the condensed state.* Oxford, United Kingdom: Pergamon

[9] Giamarchi, T. 2003. *Quantum physics in one dimension.* Oxford, United Kingdom: Oxford University Press

[10] Hansson, T. H. 2011. *Fermi and Luttinger liquids.* Lecture notes. Retrieved from http://www.fysik.su.se/~hansson/cmft/notes/Fermi_Liquids.pdf

[11] Haldane, F. D. M. 1981. *Effective harmonic-fluid approach to low-energy properties of one-dimensional quantum fields.* Phys. Rev. Lett. **47** (25), 1840

[12] Boninsegni, M., Prokof'ev N. V., Svistunov B.V. 2006. *Worm algorithm and diagrammatic Monte Carlo: A new approach to continuous-space path integral Monte Carlo simulations*, Phys. Rev. E **74** (3), 036701

[13] Boninsegni, M. 2005. *Permutation sampling in path integral Monte Carlo.* J. Low Temp. Phys. **141**(1-2), 27

[14] Pollock, E. L., Ceperley, D. M. 1987. *Path-integral computation of superfluid densities*, Phys. Rev. B **36** (16), 8343

[15] Del Maestro, A., Affleck, I. 2010. *Interacting bosons in one dimension and the applicability of Luttinger-liquid theory as revealed by path-integral quantum Monte Carlo calculations*, Phys. Rev. B **82** (6), 060515

[16] Vranješ Markić, L., Glyde, H. R. 2015. *Superfluidity, BEC, and dimensions of liquid* ^{4}He *in nanopores.* Phys. Rev. B **92** (6), 064510

[17] Vranješ Markić, L., Vrcan, H., Zuhrianda, Z., Glyde, H. R. 2017. *Superfluidity, BEC and the structure in 1D Luttinger liquids*, manuscript submitted for publication

[18] Anderson, P. W. 1958. *Absence of Diffusion in Certain Random Lattices.* Phys. Rev. **109** (5), 1492

[19] Cazalilla, M. A., Citro, R., Giamarchi, T. Orignac, E., Rigol, M. 2011. *One dimensional bosons: From condensed matter systems to ultracold gases* Rev. Mod. Phys. **83** (4), 1405

[20] Cazalilla, M. A. 2004. *Bosonizing one-dimensional cold atomic gases.* J. Phys. B **37** (7), S1

[21] Giamarchi, T., Shultz, H. J. 1988. *Anderson localization and interactions in one-dimensional metals.* Phys. Rev. B **37** (1), 325

[22] Ristivojević, Z., Petković, A., Le Doussal, P. Giamarchi, T. 2012.*Phase Transition of Interacting Disordered Bosons in One Dimension.* Phys. Rev. Lett. **109** (2), 026402

[23] Furusaki, A., Nagaosa, N. 1993 *Single-barrier problem and Anderson localization in a one-dimensional interacting electron system.* Phys. Rev. B **47** (8), 4631

[24] Kane, C. L., Fisher, P. A. 1992. *Transport in a one-channel Luttinger liquid.* Phys. Rev. Lett. **68** (8), 1220

[25] Giamarchi, T. 2016. *Quantum matter at ultralow temperatures.* Book Series: Proceedings of the International School of Physics Enrico Fermi **191**, 413

[26] Gould, H., Tobochnik, J., Christian, W. 2016. *An Introduction to Computer Simulation Methods Applications to Physical System* (3rd ed. revised). Retrieved from https://www.compadre.org/osp/document/ServeFile.cfm?ID=7375&DocID=527&Attachment=1

[27] Metropolis, N., Rosenbluth, A. W., Rosenbluth, M. N., Teller, A. H. 1953. *Equation of State Calculations by Fast Computing Machines.* J. Chem. Phys., **21** (6), 1087

[28] Doggen, E., V., H., Lemarié, G., Capponi, S., Laflorencie, N. 2017. *Weak Versus Strong Disorder Superfluid-Bose Glass Transition in One Dimension* and references therein. Preprint retrieved from arXiv:1704.02257v2.

[29] Vrcan, H. 2017. *Path integral Monte Carlo study of superfluid* ^{4}He *in disordered narrow nanopores* (master thesis). University of Split, Faculty of Science